



Modulating morphology and textural properties of Al₂O₃ for supported Ni catalysts toward plasma-assisted dry reforming of methane

Yanan Diao¹, Haiyan Wang¹, Bingbing Chen, Xiao Zhang*, Chuan Shi*

State Key Laboratory of Fine Chemicals, School of Chemical Engineering, Dalian University of Technology, Dalian 116024, China



ARTICLE INFO

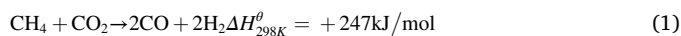
Keywords:
Ni/Al₂O₃
Morphology
Plasma coupled with catalysis
DRM reaction

ABSTRACT

The synergy between plasma and catalysis has been long noticed, but how to further improve the synergy remains challenging. Herein, a series of Ni/Al₂O₃ catalysts with different Al₂O₃ morphologies (nanorod-NR, nanosheet-NS and spherical flower-SF) were investigated for plasma-assisted dry reforming of methane (DRM). Surface properties, metal dispersion, and discharge properties were modulated, and thereby affected catalytic performance and plasma-catalysis synergistic efficiency. Sufficient surface hydroxyls on NS-Al₂O₃ dispersed and anchored Ni centers via forming Ni-O-Al linkages, and the specific two-dimensional structure facilitated charge deposition and generated a stronger local electric field. Accordingly, the Ni/NS-Al₂O₃ catalyst showed the best catalytic activity & stability and energy efficiency in the reaction. The present study provides a promising strategy to enhance the synergy and energy efficiency of plasma-catalysis by coupling highly dispersed Ni active centers and specific structures of Al₂O₃ substrate to obtain an efficient catalyst motivating the DRM reaction under mild conditions.

1. Introduction

With the increased global production of shale gas and natural gas in recent years, methane as the major component has attracted great efforts on converting it to value-added chemicals, such as aromatics, methanol and syngas [1,2]. Dry reforming of methane (DRM) reaction is regarded as one of the most promising processes to simultaneously convert the abundant greenhouse gases (CH₄ and CO₂) to syngas with a unity ratio of H₂/CO in the products (Eq. (1)). The obtained syngas is suitable to be further synthesized into the oxygenated chemicals (acetic acid and methanol etc.) and hydrocarbons (C₂H₄ and C₃H₆ etc.) by Fischer-Tropsch reaction [3]. Additionally, DRM reaction provides a direct route to convert biogas, which is mainly composed by CO₂ (25–65 %) and CH₄ (35–75 %) [4–6].



Due to the highly endothermic nature of DRM reaction, high temperatures above 700 °C is required to achieve an appreciable conversion of reactant gases [7,8]. Ni-based catalyst as one of the non-noble metal catalysts has been extensively investigated and considered as the most promising one in industrial application due to its high initial activity

comparable to noble metal catalysts and low cost [9]. Nevertheless, the major challenges of Ni-based catalysts are metal sintering and/or coke deposition at high operating temperatures, especially for the high temperature DRM reaction [10,11]. Therefore, how to effectively drive CH₄ and CO₂ activation under mild conditions is the key to solve all the above-listed catalytic issues.

With this goal in mind, several advanced technologies have been developed with the assistance of non-voluminous work, such as electric and photonic energies to effectively drive C-H activation in a controllable process, and enable such a thermodynamically restricted reaction to occur under a mild condition [12]. Given that, non-thermal plasma (NTP) coupled with catalysis has been studied to enable DRM reaction occur in a mild manner, and thus the sintering of Ni active centers might be suppressed [13,14]. Therefore, great efforts have been made on developing effective Ni-based catalysts for the plasma-catalytic DRM reaction.

The morphology of the catalyst support seems to exert a significant influence on the synergy of plasma-catalysis. For instance, compared to CeO₂ nanoparticles, an enhanced methanol conversion was attained (94.1 %) with high CO₂ selectivity (90.1 %) over CeO₂ nanorods in plasma-catalytic methanol oxidation reaction. This improvement can be

* Corresponding authors.

E-mail addresses: zhangxiao@dlut.edu.cn (X. Zhang), chuanshi@dlut.edu.cn (C. Shi).

¹ These authors contributed equally to this work.

ascribed to the abundant formation of surface oxygen vacancies on CeO₂ nanorods, thereby effectively promoting the deep oxidation of methanol [15]. In another study, Wang et al. revealed that the highest toluene conversion was obtained over α -MnO₂ catalyst with a double-tunneled structure compared to that over β -, γ - and δ -MnO₂ catalysts in plasma-assisted catalysis, which was ascribed to increase the adsorption of oxygen species (O₂, O₃) on α -MnO₂ and promote the deep oxidation of reactants during the plasma-catalytic process [16]. Also, Roland et al. found that both the porous γ -alumina and silica gel showed a higher conversion of volatile organic compounds (VOCs) and selectivity of CO₂ product compared to the non-porous alumina and silica nanoparticles, respectively. The results showed that the produced intermediates could slowly diffuse into the porous structure of packing materials to prolong the residence time, thus favor the total oxidation of VOCs [17]. In a recent study, our group discovered that Mo₂C nanorods is able to facilitate charge deposition due to the unique nanoporous structures, and a higher CO₂ turnover frequency (TOF) was obtained compared to that of the conventional Mo₂C nanoparticles [18].

For the metal-supported catalysts, Fan et al. prepared the Ni/S1 catalysts with different porous structures and found that the Ni/D-S1 catalyst with hierarchical pores had a relatively high Ni dispersion and showed the best catalytic activity, ascribing to the favored diffusion of reactive species in the micro-meso pore structure in the discharge region [19]. Additionally, the authors also investigated the influence of packing materials and suggested that the UiO-67 MOF with highly porous nature was beneficial to the generation of filamentary micro-discharge and surface discharge under plasma conditions in comparison to the reference ZrO₂ particles. Noted that the Pt NPs@UiO-67 catalyst further improved the catalytic performance due to the accelerated surface reactions [20]. Therefore, using appropriate support or catalyst, which has some specific structures to form surface discharge, is of great importance to enhance the catalytic performance of the plasma-catalysis reactions. To the best of our knowledge, few studies have been conducted to reveal the morphology effect of γ -Al₂O₃ support on Ni dispersion and the discharge properties in plasma-assisted DRM reaction, albeit that it has been widely employed in this process.

In the present work, the effects of γ -Al₂O₃ support morphologies (nanorods-NR, nanosheets-NS, and spherical flower-SF) on dispersing and stabilizing metallic Ni sites, as well as modifying the discharge properties of Ni/Al₂O₃ catalysts were illuminated to understand the synergistic effect between plasma and catalysis for the DRM reaction. The present study reveals that by coupling nonthermal plasma with specific morphology of catalysts, the synergy efficiency could be boosted, and the two-dimensional materials with priority for mass diffusion and electron transfer show more prospective.

2. Experimental section

2.1. Preparation of catalysts

2.1.1. Synthesis of Al₂O₃ support with specific morphologies

Al₂O₃ supports with different morphologies were synthesized by hydrothermal methods with slight modification reported in the published studies [21–23].

2.1.2. γ -Al₂O₃ nanosheet

firstly, 6.4 g Al(NO₃)₃·9H₂O was dissolved in 120 mL deionized water. Subsequently, 9.28 g urea was added to the solution with vigorous stirring for 30 min at room temperature. Then the mixture solution was transferred to a 100 mL Teflon-lined stainless autoclave and kept at 100 °C for 48 h. After cooling down to room temperature, the precipitate was obtained by filtration and washed thoroughly with deionized water and ethanol for three times, respectively, and then dried at 80 °C for 12 h. Finally, the powder was calcined at 600 °C in air for 2 h to obtain the γ -Al₂O₃ nanosheet, which was designated as NS-Al₂O₃.

2.1.3. γ -Al₂O₃ nanorod

8.0 g Al(NO₃)₃·9H₂O and 19.2 g urea was dissolved in 40 mL deionized water with vigorous stirring for 30 min at room temperature. Then the mixture solution was transferred to a 100 mL Teflon-lined stainless autoclave and kept at 180 °C for 20 h. After cooling down to room temperature, the precipitate was obtained by filtration and washed thoroughly with deionized water and ethanol for three times, respectively, and then dried at 80 °C for 12 h. Finally, the powder was calcined at 600 °C in air for 2 h to obtain the γ -Al₂O₃ nanorod, which was denoted as NR-Al₂O₃.

2.1.4. γ -Al₂O₃ spherical flower

7.0 g Al(NO₃)₃·9H₂O, 5.0 g glucose was dissolved in 60 mL deionized water with vigorous stirring for 30 min at room temperature. Then the mixture solution was transferred to a 100 mL Teflon-lined stainless autoclave and kept at 180 °C for 20 h. After cooling down to room temperature, the precipitate was obtained by filtration and washed thoroughly with deionized water and ethanol for three times, respectively, and then dried at 80 °C for 12 h. Finally, the powder was calcined at 600 °C in air for 2 h to obtain the γ -Al₂O₃ spherical flower, which was denoted as SF-Al₂O₃.

2.1.5. Synthesis of Ni/Al₂O₃ catalysts with different morphologies

The Ni/Al₂O₃ catalysts with different support morphologies were prepared by the incipient wetness impregnation method. Typically, γ -Al₂O₃ support was incipiently impregnated with an aqueous solution of Ni(NO₃)₂·6H₂O and then placed at room temperature for 24 h. Finally, the obtained precursor was dried overnight at 110 °C and then calcined in air at 500 °C for 4 h. The nominal loading of Ni is 10 wt % for all Ni/Al₂O₃ catalysts. The obtained Ni/Al₂O₃ nanosheet, Ni/Al₂O₃ nanorod and Ni/spherical flower-like Al₂O₃ catalysts were designated as Ni/NS-Al₂O₃, Ni/NR-Al₂O₃, Ni/SF-Al₂O₃, respectively.

2.2. Catalyst characterization

2.2.1. XRD

X-ray diffraction (XRD) patterns were recorded on an XRD-6000 (Shimadzu, Kyoto, Japan) with Cu K α radiation source ($\lambda = 0.1542$ nm), and operated at 30 kV and 30 mA. The step-scan was taken over the 20 in the range of 20–90° with a scanning rate of 10°/min. Crystallographic information was obtained by comparing the obtained XRD patterns to the Joint Committee on Powder Diffraction Standards (JCPDS).

2.2.2. BET surface area

The specific surface area of synthesized Ni/Al₂O₃ catalysts was calculated by Brunauer-Emmett-Teller method on Micromeritics ASAP 2460 analyzer. The pore volume and pore size of them were also measured on the same instrument. Prior to N₂ adsorption-desorption at –196 °C, all catalysts were degassed in vacuum at 200 °C for 4 h.

2.2.3. TEM

Transmission Electron Microscope (TEM) images were recorded on a Tecnai G2 F30 S-Twin system (Thermo Scientific, America) operated at 300 kV. Prior to the measurement, the catalyst was dispersed in absolute ethanol for 30 min under ultra-sonication condition and subsequently dripped on a copper grid.

2.2.4. SEM

Scanning electron microscopic (SEM) images were obtained using the QUANTA 45 equipment (FEI company, America) operated at 30 kV. The Al₂O₃ supports were supported on a thin Au layer prior to the measurement.

2.2.5. ²⁷Al MAS NMR

²⁷Al MAS NMR spectra were recorded on the Agilent DD2–500 MHz

spectrometer equipped with a 4 nm probe (a spinning rate of 14 kHz) and operated at 130.2 MHz. All measured spectra were referenced to 1 % Al(NO₃)₃ aqueous solution and accumulated for 200 scans with a π/12 flip angle and 2 s pulse delay.

2.2.6. FT-IR

The diffuse reflectance infrared Fourier transform (FT-IR) spectra were recorded on a Bruker Tensor 27 spectrometer equipped with MCT detector. The sample was pretreated at 200 °C for 30 min in He flow before FT-IR measurements. A background spectrum was recorded at 30 °C under He flow. And then the FT-IR spectra subtracted the background spectrum and were recorded accumulated for 60 scans with a resolution of 4 cm⁻¹ at 30 °C under He flow.

2.2.7. Py-IR

The pyridine adsorption-infrared (Py-IR) spectra were measured using a Bruker Tensor 27 spectrometer equipped with a vacuum chamber. The samples were pretreated at 200 °C for 30 min under vacuum condition before pyridine adsorption. All Py-IR spectra of samples were recorded at 150 °C accumulated for 60 scans with a resolution of 4 cm⁻¹.

2.2.8. H₂-TPR

Hydrogen temperature-programmed reduction (H₂-TPR) measurements were performed on a Micromeritics AutoChem II 2920 chemisorption analyzer. 0.1 g catalyst was loaded in a U-shape quartz reactor. The catalyst was purged at 300 °C for 30 min in Ar (30 mL/min), and then cooled down to 30 °C. Subsequently, the pretreated catalyst was heated from 30 to 800 °C in 5 % H₂/Ar (100 mL/min) at a ramping rate of 10 °C/min.

2.2.9. H₂ chemisorption

H₂ pulse chemisorption experiments were performed on a Micromeritics AutoChem II 2920 chemisorption analyzer. Firstly, the catalyst was reduced with 50 vol% H₂/Ar (100 mL/min) at 650 °C for 1 h, and followed by purging in Ar (50 mL/min) for 30 min before cooling down to 0 °C. Next, the H₂ pulse was injected repeatedly until the peak area of the H₂ pulse kept constant. The amounts of exposed Ni atoms were calculated by assuming the stoichiometry factor of Ni-H equal to 1.

2.2.10. TG-DTA

Thermogravimetric-differential analysis (TG-DTA) was performed on a TGA/SDTA851e thermobalance (Mettler Toledo) for spent catalysts. Prior to the test, 15 mg spent catalyst was pretreated by Ar at 200 °C for 1 h and then cooling down to 50 °C. After that, the temperature was increased from 50 to 800 °C with a ramping rate of 10 °C/min in static air flow to measure the weight loss of the spent catalyst.

2.3. Catalytic activity evaluation

2.3.1. Thermal-catalytic performance tests

The thermal-catalytic activity for the DRM reaction was evaluated in a fixed-bed reactor (Fig. S1). Typically, 18.75 mg catalyst (40–60 mesh) mixed with quartz sands was placed between quartz wool plugs in a quartz tube with inner diameter of 6 mm. The catalyst was firstly reduced by H₂ (100 mL/min) at 650 °C for 1 h. After cooling down to 600 °C, the mixed reactants of CH₄ and CO₂ (CH₄/CO₂ = 1/1) with a total flow rate of 75 mL/min was introduced, corresponding to weight hourly space velocity (WHSV) of 240,000 mL/g/h, and then the activity test was carried out from 600 to 800 °C with temperature increment of 50 °C. The effluents were analyzed by an online gas chromatograph (Model GC 7900, Tianmei, China) equipped with thermal conductivity detector (TCD) and flame ionization detector (FID).

2.3.2. Plasma-catalytic performance tests

The plasma-catalytic activity of Ni/Al₂O₃ catalysts was evaluated in

a fixed-bed DBD reactor (Fig. S1). Typically, 10 mg catalyst (40–60 mesh) diluted with 440 mg quartz sands (40–60 mesh) was placed between two plug of quartz wool to form a 10 mm catalyst bed inside a corundum tube. Prior to the experiment, the catalyst was pretreated by H₂ (100 mL/min) at 650 °C for 1 h. The feed gas mixture was passed through the tube without external heating at a total flow rate of 100 mL/min (CH₄/CO₂/Ar = 3/3/2) with an input power of ca. 50 W, corresponding to a WHSV of 600,000 mL/g/h. The effluents were analyzed by an online gas chromatograph (Model GC 7900II, Tianmei, China) equipped with thermal conductivity detector (TCD) and flame ionization detector (FID) after running the reaction for 200 min. Additionally, the stability test of the Ni/NS-Al₂O₃ catalyst was performed with an input power of ca. 50 W at a WHSV of 100,000 mL/g/h with no external heating.

2.3.3. Several calculations used for catalytic reaction

The CH₄ conversion (X_{CH_4}), CO₂ conversion (X_{CO_2}), CO selectivity (S_{CO}), H₂ selectivity (S_{H_2}), H₂/CO ratio, Carbon balance ($C_{balance}$) and discharge power ($P_{discharge}$) were calculated as follows:

$$X_{CH_4}(\%) = \frac{F_{CH_4,in} - F_{CH_4,out}}{F_{CH_4,in}} \times 100\% \quad (2)$$

$$X_{CO_2}(\%) = \frac{F_{CO_2,in} - F_{CO_2,out}}{F_{CO_2,in}} \times 100\% \quad (3)$$

$$S_{CO}(\%) = \frac{F_{CO,out}}{(F_{CH_4,in} - F_{CH_4,out}) + (F_{CO_2,in} - F_{CO_2,out})} \times 100\% \quad (4)$$

$$S_{H_2}(\%) = \frac{F_{H_2,out}}{2(F_{CH_4,in} - F_{CH_4,out})} \times 100\% \quad (5)$$

$$H_2 / CO = \frac{F_{H_2,out}}{F_{CO,out}} \times 100\% \quad (6)$$

$$C_{balance}(\%) = \frac{F_{CO,out}}{(F_{CH_4,in} - F_{CH_4,out}) + (F_{CO_2,in} - F_{CO_2,out})} \times 100\% \quad (7)$$

$$P_{discharge} = f \int_0^T u dQ \quad (8)$$

Where F_{in} and F_{out} refer to the flow rate of inlet and outlet gases (unit: mL/min), respectively; f refers to the frequency of discharge (unit: Hz); Q refers to the charge of discharge (unit: C); u refers to the applied voltage (unit: V).

The amount of normalized carbon deposition on spent catalyst after stability test was calculated by the following formula:

$$\text{Normalized carbon deposition} = \frac{n_{\text{carbon deposition}}}{(n_{\text{converted CH}_4}^* + n_{\text{converted CO}_2}^*) \times m_{\text{cat}}} \quad (9)$$

Where $n_{\text{carbon deposition}}$ refers to moles of carbon deposition measured by TG-DTA plots (unit: mmol); $n_{\text{CH}_4,\text{converted}}^*$ and $n_{\text{CO}_2,\text{converted}}^*$ refer to moles of converted CH₄ and CO₂ (unit: mol), respectively; m_{cat} refers to the mass of spent catalyst (unit: g).

The energy efficiency (EE) of the reactor and the fuel production efficiency (FPE) were calculated according to the following formulas [24]:

$$EE = \frac{n_{\text{CH}_4,\text{converted}} + n_{\text{CO}_2,\text{converted}}}{P_{\text{discharge}}} \quad (10)$$

$$FPE(\%) = \frac{n_{\text{CO},\text{converted}} \times LHV_{\text{CO}} + n_{\text{H}_2,\text{converted}} \times LHV_{\text{H}_2}}{n_{\text{CH}_4,\text{converted}} \times LHV_{\text{CH}_4} + P_{\text{discharge}}} \times 100\% \quad (11)$$

Where $n_{\text{CH}_4,\text{converted}}$ and $n_{\text{CO}_2,\text{converted}}$ refer to the moles of converted CH₄ and CO₂ per minute (unit: mol/s), respectively. LHV_{CO} , LHV_{H_2} and LHV_{CH_4} refer to the low heating value of CO, H₂ and CH₄ (unit: J/mol), respectively. $P_{\text{discharge}}$ refers to discharge power (unit: W).

2.3.4. Kinetic measurements

Determination of turnover frequency (TOF). For thermal-catalytic DRM reaction, the turnover frequency of CH₄ (TOF_{CH₄}) was measured at 800 °C over in the kinetics-controlled regime to exclude gas diffusion, which need to control the CH₄ conversion below 20 % at a WHSV of 2,500,000 mL/g/h. The specific reaction rate of CH₄ (r_{CH₄}) and TOF_{CH₄} of catalysts were calculated as follows:

$$r_{\text{CH}_4} = \frac{F_{\text{CH}_4,\text{in}} \times X_{\text{CH}_4}}{m_{\text{cat}} \times 22400 \times 60} \quad (12)$$

$$\text{TOF}_{\text{CH}_4} = \frac{r_{\text{CH}_4}}{\text{amount of exposed Ni atoms}} \quad (13)$$

Where, m_{cat} refers to catalyst mass (unit: g), and the amount of exposed Ni atoms is measured by H₂ pulse, respectively.

2.3.5. Determination of apparent activation energy (E_{a, plasma})

The apparent activation energy (E_{a, plasma}) of the plasma-assisted DRM reaction for CO₂ conversion was measured according to the calculated method reported in the literature [25,26]. Typically, 6 mg catalyst mixed with 444 mg quartz sands was placed between two plug of quartz wool to form a 10 mm height inside a corundum tube. Before the test, the catalyst was reduced by H₂ (100 mL/min) at 650 °C for 1 h. After the pretreatment, the plasma-catalytic test was performed at 500 °C and increased the discharge power from 6 W to 29 W. Additionally, in order to control the CO₂ conversion below 20 %, the corresponding WHSV was fixed at 1,000,000 mL/g/h. In this test, the effluent gases from the outlet were analyzed by an online gas chromatograph (Model GC 7900II, Tianmei, China) equipped with thermal conductivity detector (TCD) and flame ionization detector (FID) after running the reaction for 1 h. The specific reaction rate of CO₂ (r_{plasma-cat, CO₂}) and activation energy for CO₂ conversion (E_{a, plasma-cat, CO₂}) in plasma-catalytic DRM reaction were calculated by the following formulas:

$$r_{\text{plasma-cat, CO}_2} = \frac{F_{\text{CO}_2,\text{in}} \times X_{\text{CO}_2}}{m_{\text{cat}} \times 22400 \times 60} \quad (14)$$

$$r_{\text{plasma-cat, CO}_2} = A \times e^{-\frac{E_{a, \text{plasma-cat, CO}_2}}{R} \times \frac{P_{\text{dis}}}{P_{\text{total}}}} \quad (15)$$

Where A, F_{total}, P_{dis} and E_{a, plasma-cat, CO₂} refer to the pre-exponential factor, the total flow rate (unit: mL/min), discharge power and the apparent activation energy for CO₂ conversion (unit: kJ/mol), respectively.

2.3.6. Plasma characterizations

Four metrics of current were calculated to characterize the discharge behavior for plasma-assisted DRM reaction, namely, the time-averaged discharge current (I_d), the number of discharge in a given half-cycle (N_d), the average discharge magnitude (current peak height, h_d) and the lifetime of the discharge current (τ_d). The average discharge magnitude and the lifetime of the discharge current for each discharge were evaluated in view of the current peak height and full width at half maximum (FWHM) for a measured peak in the oscillogram, respectively. Additionally, the four metrics were evaluated independently for the positive and negative half-cycles because of the asymmetric electrical signal produced by the asymmetry of the DBD plasma (with only one electrode covered by a dielectric), and defined as follows [18,27].

$$I_d = \frac{2}{\tau} \int_0^{\tau/2} I_d^*(t) dt \quad (16)$$

$$N_d = \sum_0^{\tau/2} N_d^*(t) \quad (17)$$

$$h_d = \frac{\sum_{i=1}^{N_d} h_d(i)}{N_{\tau/2}} \quad (18)$$

Where, τ, I_d^{*}, N_d^{*} and h_d refer to the cycle period, the real-time discharge current in per half cycle (unit: mA), the number of discharge and the height of each peak in per half cycle, respectively. The metric (τ_d) is the average lifetime of each discharge for the positive and negative half cycles (unit: μs), which is evaluated based on FWHM analysis.

3. Results and discussion

3.1. Characterization of the catalysts

N₂ adsorption-desorption isotherms and pore size distribution of the as-prepared Ni/NS-Al₂O₃, Ni/SF-Al₂O₃ and Ni/NR-Al₂O₃ catalysts were shown in Fig. 1. For the Ni/SF-Al₂O₃ catalyst, a typical type IV isotherm was detected with a H1 hysteresis loop at the relative pressure range (P/P₀) of 0.4–0.9, suggesting the presence of mesoporous structure (Fig. 1 (A)) [28]. Further observation in detail pore size distribution showed regular mesoporous characteristics with a pore size center at ca. 6.2 nm for Ni/SF-Al₂O₃ catalyst (Fig. 1(B)), thus possessing the largest specific surface area of 176 m²/g among these three catalysts (Table 1). Unlike the Ni/SF-Al₂O₃ catalyst, both Ni/NS-Al₂O₃ and Ni/NR-Al₂O₃ catalysts showed mixed isotherms of type II and IV with a H3 hysteresis loop at the relative pressure range (P/P₀) of 0.5–1.0, indicating the presence of slit-like pores in the catalysts [29,30]. Correspondingly, both Ni/NS-Al₂O₃ and Ni/NR-Al₂O₃ catalysts exhibited a broad mixed distribution feature of few mesopores and dominant macropores, mainly ascribed to the slit-like pores, and showed the surface area of 158 and 101 m²/g, respectively. In addition, benefit from the abundant slit-like pores, Ni/NS-Al₂O₃ catalyst possessed the largest pore volume (0.43 cm³/g), followed by the Ni/NR-Al₂O₃ catalyst of 0.31 cm³/g. Owing to the ordered mesopores, relatively smaller pore volume was obtained over the Ni/SF-Al₂O₃ catalyst (0.20 cm³/g).

H₂-TPR experiment was carried out to study the reducible behavior of the as-prepared NiO/Al₂O₃ catalysts, as shown in Fig. 1(C). For NiO/NR-Al₂O₃ catalyst, there were two main reduction peaks centered at ca. 393 and 534 °C, which can be ascribed to surface NiO species and interacted NiO species with NR-Al₂O₃ support, respectively [31]. In addition, the weak peak centered at 820 °C was observed because of the reduction of NiAl₂O₄ in the catalyst. While, for the NiO/SF-Al₂O₃ and NiO/NS-Al₂O₃ catalysts, the reduction temperature of the interacted NiO species moved from 534 °C up to 707 °C and 668 °C, respectively, suggesting an enhanced interaction between nickel and SF-Al₂O₃ and NS-Al₂O₃ supports. Similarly, a high temperature reduction peak at 821 °C was also observed over the Ni/NS-Al₂O₃ catalyst, which can be ascribed to Ni²⁺ reduction of NiAl₂O₄ spinel [32]. Owing to the stronger interaction and the existing of NiAl₂O₄ species, the Ni/NS-Al₂O₃ and Ni/SF-Al₂O₃ catalysts exhibited lower reduction degree of 49 % and 40 % after reduction at 650 °C, respectively, compared with that of 82 % for the Ni/NR-Al₂O₃ catalyst, shown in Table 1.

To further identify the phase structure of the pre-reduced NiO/Al₂O₃ catalysts, the X-ray powder diffraction (XRD) patterns were shown in Fig. 1(D). The characteristic diffraction peaks ascribed to γ-Al₂O₃ (JCPDS No.75-0921) and NiAl₂O₄ phases (JCPDS No.10-0339) were observed for all catalysts. It was worth noticing that the evidently characteristic diffraction peak of metallic Ni (JCPDS No.70-0989) at 44.6° was observed for the reduced Ni/NR-Al₂O₃ catalyst although the overlapped peak shown for the Ni and Al₂O₃ species from 42° to 49°, suggesting that large Ni nanoparticles existed on the catalyst. While, for the Ni/NS-Al₂O₃ and Ni/SF-Al₂O₃ catalysts, there were no obvious diffraction peaks of metallic Ni, which implied that Ni was highly dispersed (ca. < 5 nm) over the NS-Al₂O₃ and SF-Al₂O₃ supports. The above results are in good agreement with the H₂-TPR results, which indicate that the weak interaction of NiO with NR-Al₂O₃ caused a severe

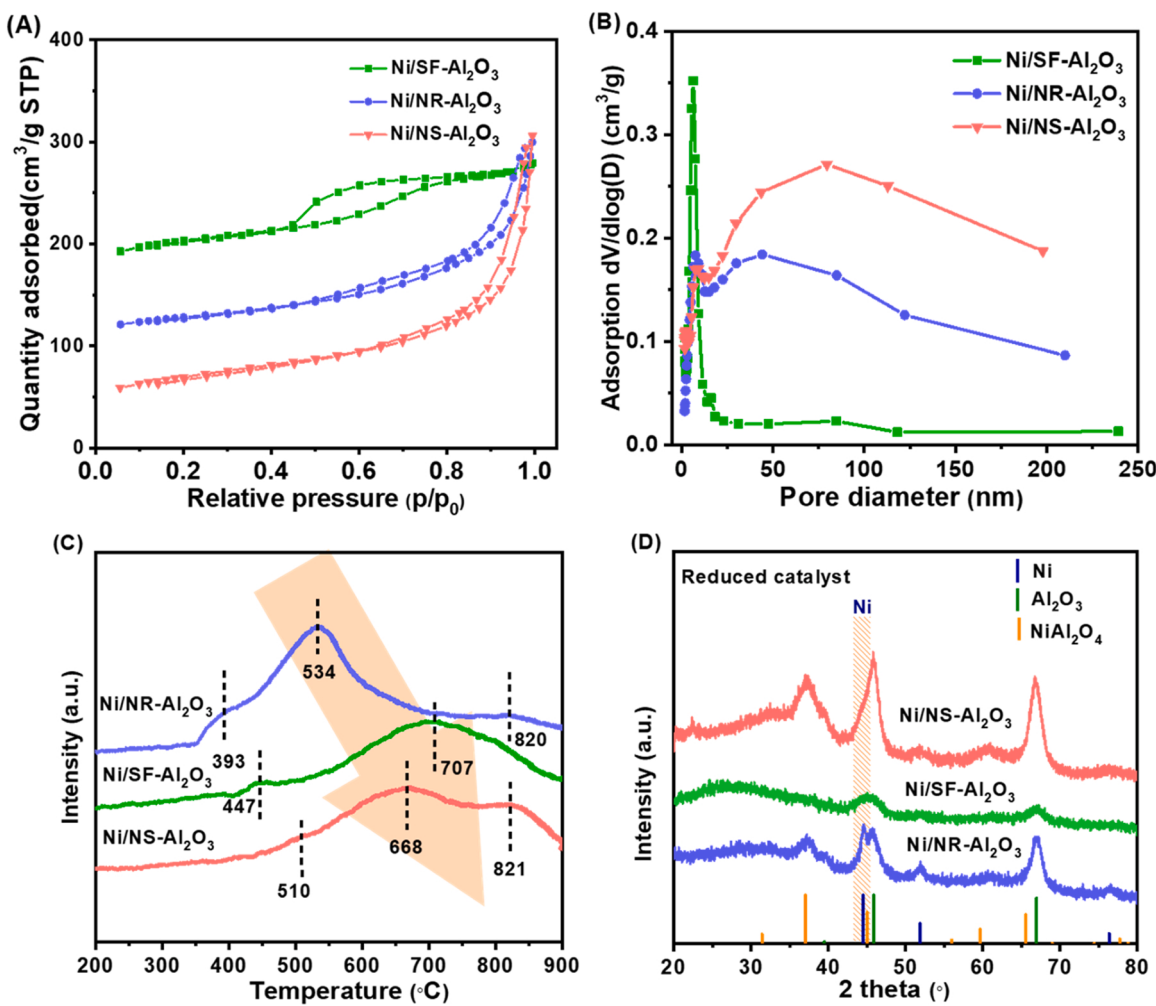


Fig. 1. (A) N₂ adsorption-desorption isotherms and (B) pore size distribution, (C) H₂-TPR profiles of the fresh Ni/Al₂O₃ catalysts with different support morphologies; (D) XRD patterns of reduced Ni/Al₂O₃ catalysts with different morphologies.

Table 1
Textural properties of Ni/Al₂O₃ catalysts with different support morphologies.

Catalyst	S _{BET} (m ² /g) ^a	Pore volume (cm ³ /g) ^a	Average pore size (nm) ^a	Particle size (nm) ^b	Reduction degree (%) ^c	Number of exposed Ni atoms (μmol/g _{cat}) ^d
Ni/NS-Al ₂ O ₃	158	0.43	11.0	4.3	49	21.52
Ni/SF-Al ₂ O ₃	176	0.20	4.5	5.9	40	16.93
Ni/NR-Al ₂ O ₃	101	0.31	9.5	11.5	82	15.73

^a Determined by N₂ adsorption-desorption isotherms.

^b Determined by size distribution of Ni particles on the reduced catalysts obtained from TEM images.

^c Determined by H₂-TPR profiles of the fresh catalysts.

^d Determined by H₂ pulse chemisorption experiments.

Ni particle growth (or agglomeration) upon reduction, while the strong metal-support interaction would generate better Ni dispersion after the reduction.

TEM images were shown to characterize the morphology characteristics of the supports and metallic Ni dispersion over different Ni/Al₂O₃ catalysts. As depicted in Figs. S2–3, we can see that different

morphologies of Al₂O₃ supports were successfully synthesized via hydrothermal methods. The metallic Ni nanoparticles (NPs) shown as dark spots with an obvious contrast to that of Al₂O₃ supports, and the size distributions of Ni NPs were counted shown in Fig. 2. According to the statistical results, it can be seen that the dispersed Ni nanoparticles on the reduced Ni/NS-Al₂O₃ and Ni/SF-Al₂O₃ has an average particle size of ~4.3 and ~5.9 nm, respectively. While, a much larger particles of ~11.2 nm was observed on the reduced Ni/NR-Al₂O₃, which was in agreement with XRD results (Fig. 1(D)). It is clear that the morphologies of Al₂O₃ supports exert a significant influence on the dispersion of metallic Ni. The number of exposed Ni atoms was measured by hydrogen chemisorption, and as listed in Table 1 that the Ni/NS-Al₂O₃ catalyst exhibited the highest value of exposed Ni compared with two other catalysts, which may be related to the Ni NPs size and the reduction degree of Ni²⁺ species [31], and it was consistent with the above characterizations results, suggesting that the optimal dispersion of metallic Ni was induced over the Al₂O₃ support with the nanosheet structure.

3.2. Dispersion mechanism of Ni over Al₂O₃ supports with different morphologies

In order to better understand the dispersion states of metallic Ni in terms of Al₂O₃ supports with different morphologies, ²⁷Al solid-state MAS NMR spectra and FT-IR spectra were recorded as shown in Fig. 3. There were two characteristic ²⁷Al NMR peaks centered at 10 and 67 parts per million (ppm) chemical shifts over the three Al₂O₃ supports,

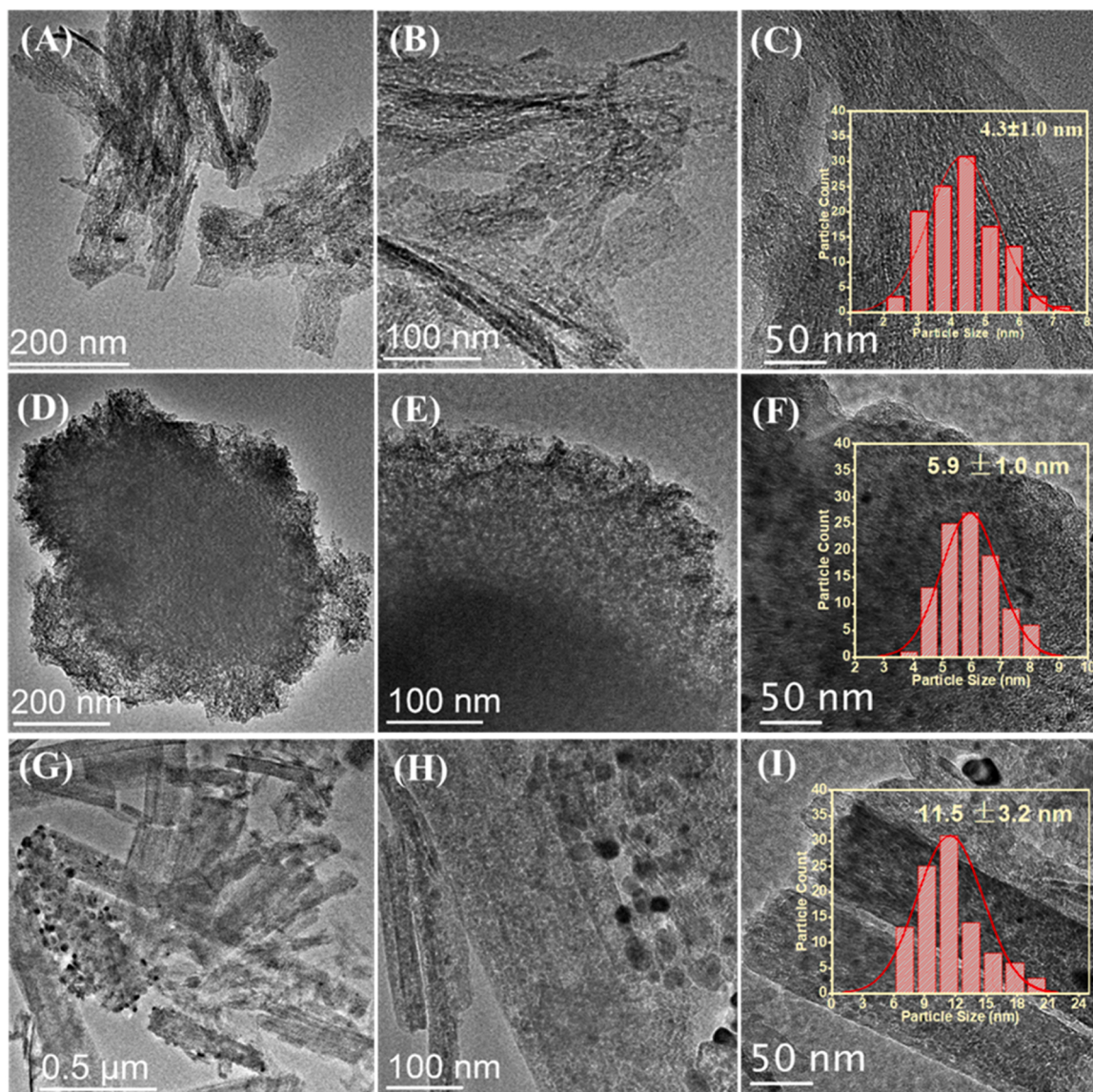


Fig. 2. TEM images of the reduced (A-C) Ni/NS-Al₂O₃, (D-F) Ni/SF-Al₂O₃ and (G-I) Ni/NR-Al₂O₃ catalysts and Ni particle size distribution of the corresponding catalysts (insert).

which belonged to Al³⁺ cations in octahedral (Al³⁺_{octa}) and tetrahedral (Al³⁺_{tetra}) coordination, respectively (Fig. 3(A)). Interestingly, a third ²⁷Al NMR peak centered at 35 ppm was observed on SF-Al₂O₃ support, which represented Al³⁺ cations at the unsaturated pentahedral coordination (Al³⁺_{penta}) [33–35]. We can deduce that the distinct coordinate environments of Al³⁺ cations on Al₂O₃ supports were observed due to different morphologies and preparation conditions. Moreover, the peak intensity of Al³⁺_{penta} decreased after Ni impregnation (Fig. 3(A)), and the percentage of Al³⁺_{penta} sites decreased from 15.0 % on pure SF-Al₂O₃ to 10.0 % (Fig. S4), indicating that the coordinately unsaturated Al³⁺_{penta} provided partial sites for Ni coordination to disperse [35], rendering metal-support interaction between Ni and the Al₂O₃ support. However, such coordination cannot be observed over the other two supported Ni samples.

Furthermore, FT-IR experiments were performed to study the surface groups of the Ni/Al₂O₃ samples. As displayed in Fig. 3(B), three peaks centered at ca. 3580, 3678, and 3730 cm⁻¹ were clearly presented for the NS-Al₂O₃ support corresponding to the hydroxyl groups coordinated to Al³⁺ cations in octahedral interstices, a bridging hydroxyl group linked with tetrahedral and octahedral Al³⁺ cations, respectively [36–38]. When Ni was loaded on the NS-Al₂O₃ support, a decreased

peak intensity of hydroxyl groups at 2600–3800 cm⁻¹ was observed, indicating the consumption of hydroxyl groups during the preparation process due to the interaction between Ni²⁺ and hydroxyl sites (Fig. 3(B)) [39], which facilitated the high dispersion of metallic Ni. Similarly, Freund reported that the surface hydroxyl groups on a Al₂O₃ film mediate a strong interaction with metallic Ru [40]. By contrast, there were a weak peak (3745 cm⁻¹) detected for SF-Al₂O₃ and NR-Al₂O₃ (attributed to the structural hydroxyl groups located in the bulk phase of Al₂O₃), indicating the lack of sufficient surface hydroxyl groups over these two supports. While due to the lack of Al³⁺_{penta} sites and limited amount of OH groups over the Ni/NR-Al₂O₃ catalyst, the poorest Ni dispersion was obtained (Fig. 2(G-I)).

Py-IR spectra of the catalysts were shown in Fig. 3(C). The peaks centered at 1445 and 1450 cm⁻¹ corresponded to the Pyridine adsorbed on Lewis acid sites (L) of Al₂O₃ supports. And the peaks centered at 1540 and 1590 cm⁻¹ were assigned to the Brønsted acid sites (B) [41–43]. For the Al₂O₃ supports, the coordinatively unsaturated Al³⁺ (Al³⁺_{penta}) acted as Lewis acid sites (L), and the hydroxyl groups on the surface provided Brønsted acid sites (B). It was clearly seen that a higher B/L ratio of 28.9 was obtained over the NS-Al₂O₃ support, which was consistent with the abundant surface hydroxyl groups (Fig. 3(B)). While, the SF-Al₂O₃

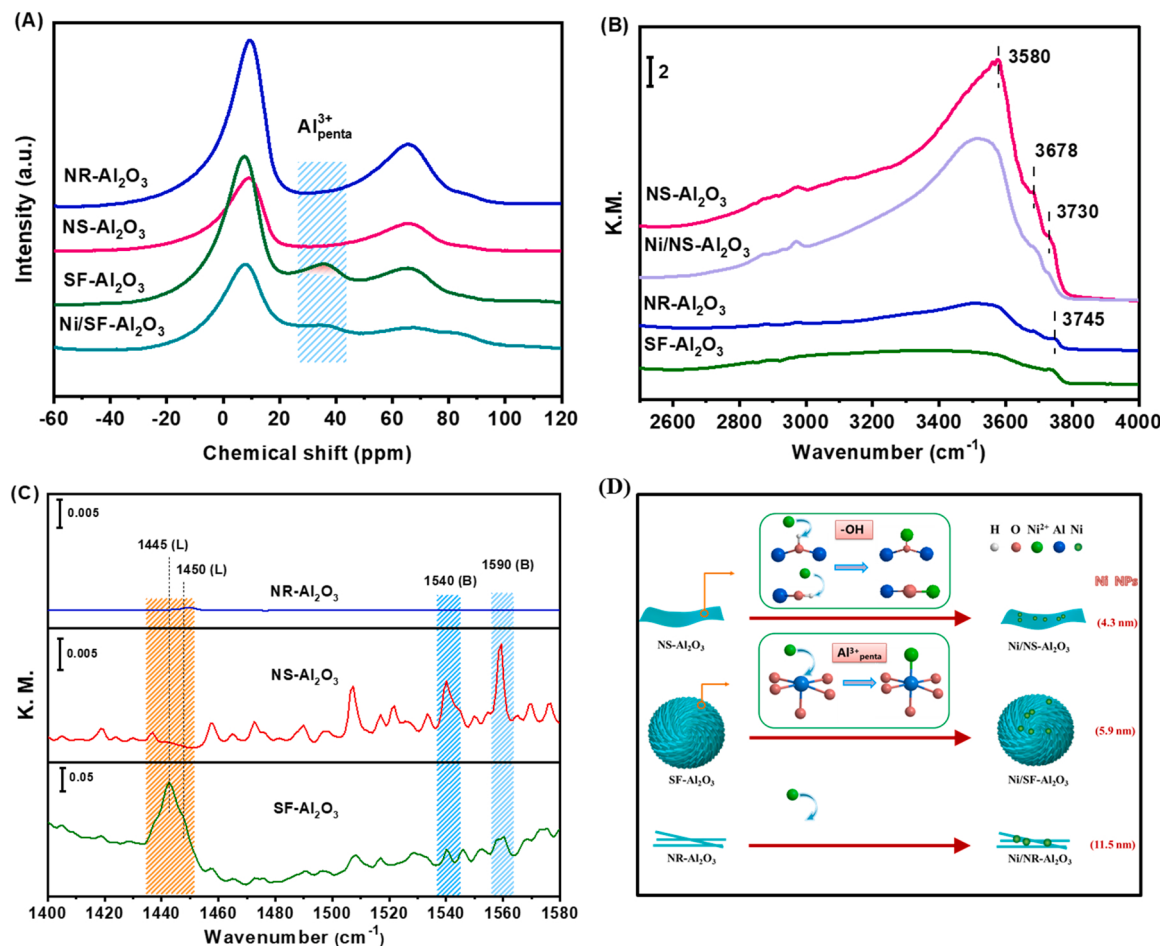


Fig. 3. (A) ^{27}Al MAS NMR spectra and (B) FTIR spectra of Al_2O_3 supports with different morphologies; (C) Py-IR spectra of Al_2O_3 supports with different morphologies at 150 °C; (D) Schematic illustration of dispersion mechanism of Ni species on Al_2O_3 with different morphologies.

support had lowest B/L ratio of 0.283, corresponding to its higher amounts of $\text{Al}^{3+}_{\text{penta}}$ (Fig. 3(A)). In contrast, a very weak peak at 1451 cm^{-1} was observed, indicating only a trace of L acid sites were existed on the NR- Al_2O_3 support. The Py-IR results were in good agreement with ^{27}Al MAS NMR and FT-IR results (Fig. 3(A-B)).

Based on the foregoing, the variation of surface properties in different Al_2O_3 supports could affect the interaction between Al_2O_3 and metallic Ni. With sufficient unsaturated Al^{3+} sites acting as binding sites and hydroxyl groups (strong chemical interaction with active metal) of the Al_2O_3 supports, active Ni species could effectively anchor and disperse on Al_2O_3 via forming Ni-Al or/and Ni-O bonds because of the strong interaction with $\text{Al}^{3+}_{\text{penta}}$ and Al-OH groups, which greatly enhanced the dispersion of Ni and the interactions with supports. Similar result has also been reported in the literature. For example, Song et al. found that the dispersed Ru nanoparticles could anchor on $\text{Al}^{3+}_{\text{penta}}$ sites of the coordinatively unsaturated Al_2O_3 support via forming Ru-Al and Ru-O bonds [44]. Zeng et al. revealed that the terminal hydroxyl groups on nanosized $\gamma\text{-Al}_2\text{O}_3$ mainly anchored Ag species through the interaction between Ag species and O atom in hydroxyl groups [39].

3.3. Catalytic performance in thermal-catalytic DRM reaction

The thermal-catalytic performance of Ni/ Al_2O_3 catalysts with different morphologies was investigated in the temperature range of 600–800 °C with CH_4/CO_2 ratio of 1/1 and a WHSV of 240,000 mL/g.h. As shown in Fig. 4(A-B), the conversions of CH_4 and CO_2 increased with the increased temperature from 600 to 800 °C for all catalysts. Meanwhile, the conversion of CH_4 was lower than that of CO_2 over the whole

temperature range owing to simultaneously occurred reverse water gas shift (RWGS) reaction [45]. For various Ni/ Al_2O_3 catalysts, the activity increased in the order of Ni/NR- Al_2O_3 < Ni/SF- Al_2O_3 < Ni/NS- Al_2O_3 . Especially, the Ni/NS- Al_2O_3 catalyst with two-dimensional structure and smaller Ni NPs of ~4.3 nm displayed the best catalytic activity during the process of thermal-catalytic DRM reaction.

The turnover frequency of CH_4 (TOF $_{\text{CH}_4}$) of Ni/ Al_2O_3 catalysts was measured in the kinetic region at 800 °C (Fig. S6 showed the variation of reaction rate with WHSV to ascertain the kinetic region), shown in Fig. 4(C). It is obvious that the TOF $_{\text{CH}_4}$ of the Ni/NS- Al_2O_3 catalyst was 161 s^{-1} , which was significantly higher than those of Ni/SF- Al_2O_3 (108 s^{-1}) and Ni/NR- Al_2O_3 (85 s^{-1}) catalysts. Moreover, a negative correlation between TOF $_{\text{CH}_4}$ and particle size of metallic Ni was established (Fig. 4(C)). The results showed that the highest TOF $_{\text{CH}_4}$ was obtained over the Ni/NS- Al_2O_3 catalyst with the smallest Ni NPs of 4.3 nm, which was consistent with literature reports [46,47]. The above results confirmed the structure sensitive nature of Al_2O_3 -supported Ni catalysts towards DRM reaction.

3.4. Catalytic performance of Ni/NS- Al_2O_3 catalyst in plasma-catalytic DRM reaction: the effects of input power

The Ni/NS- Al_2O_3 was chosen as the representative catalyst to further investigate the effect of input power towards activity and product selectivity under plasma-catalysis condition. Fig. 5(A) showed the Lissajous curves of the discharge with different input powers over the Ni/NS- Al_2O_3 catalyst. It was found that the discharge mode was transformed from filamentary discharge at lower input powers (below

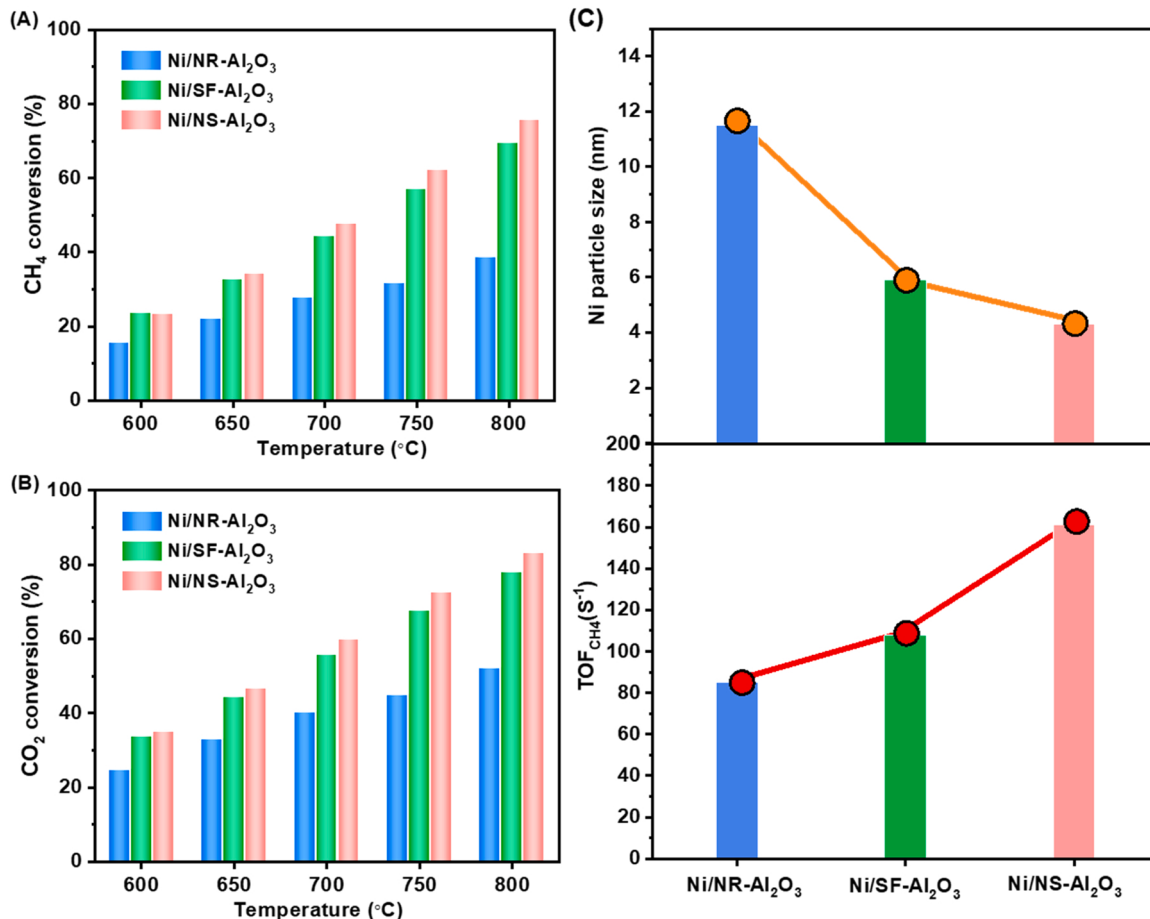


Fig. 4. (A-B) Thermal-catalytic activity of Ni/ Al_2O_3 catalysts with different support morphologies for DRM reaction. Reaction conditions: WHSV = 240,000 mL/g/h, m = 18.75 mg cat + quartz sands, $\text{CH}_4/\text{CO}_2 = 1/1$. (C) The correlation between Ni particle size and CH_4 turnover frequency (TOF) over Ni/ Al_2O_3 catalysts. Reaction conditions: $\text{CH}_4/\text{CO}_2 = 1$, T = 800 $^{\circ}\text{C}$, WHSV = 2,500,000 mL/g/h, m = 3 mg cat. + 197 mg quartz sands.

34.4 W) to surface discharge at higher input power, as determined by the shape changes of the Lissajous curves from a parallelogram to an oval-like graph [18]. Meanwhile, the actual temperature of reactor (on the outer side of tube) was measured and displayed in Fig. S7, and the results showed that the temperature increased from 113 to 766 $^{\circ}\text{C}$ as increasing the input power from 26.7 to 63.7 W without any extra heating, which originated from the utilization of heat released by the plasma [48,49].

As shown in Fig. 5(B-C), it was observed that the conversion of CH₄ was higher than that of CO₂ at the input power of 26.7 W. The highest value of H₂/CO ratio (1.48) was obtained at this input power and the higher C₂-C₃ selectivity was obtained. These results implied that the plasma induces the gas-phase reaction below 34.4 W and causes complex products and lower the CO selectivity. With increasing the input power up to 34.4 W, the conversion of CH₄ slightly decreased, and its value was lower than CO₂ conversion, and the H₂/CO ratio dropped sharply to 0.63, which suggested the co-occurrence of RWGS reaction. As the input power further raised from 34.4 to 63.7 W, the conversions of CH₄ and CO₂ simultaneously enhanced, indicating that the DRM reaction dominates at these input powers. Remarkably, the conversion of CH₄ was approximately equal to that of CO₂ at 63.7 W, and the H₂/CO ratio was close to unity (0.96), indicating that a balanced rate between CH₄ dissociation and CO₂ activation was achieved in the plasma-catalysis coupled DRM reaction under this condition.

3.5. Comparison of Ni/ Al_2O_3 catalysts with different morphologies in plasma coupled catalysis DRM reaction

The discharge properties of Ni/ Al_2O_3 samples were compared to study the effects of the support morphology and Ni dispersion (Fig. 6). The discharge power and the effective capacitance of the different Ni/ Al_2O_3 catalysts at a similar input power (ca. 55 W) were shown in Fig. 6 (A). Obviously, a similar discharge power of ca. 44–45 W was obtained over these three samples while applying the same input power (Table 2). The effective capacitance over catalysts was calculated using the method reported by Tu et al. (Fig. S8) [50]. While distinct effective capacitances were observed in which the Ni/NS- Al_2O_3 sample with the smallest Ni NPs and two-dimensional structure showed the highest effective capacitance (161 pF), which is significantly higher than that of Ni/SF- Al_2O_3 (81 pF) and Ni/NR- Al_2O_3 (70 pF). And the strongest current density and highest amplitude of current signals over Ni/NS- Al_2O_3 catalyst were observed compared to that of Ni/NR- Al_2O_3 and Ni/SF- Al_2O_3 samples during discharge (Fig. 6(B-D)), indicating the enhanced intensity of current pulses over the Ni/NS- Al_2O_3 catalyst [51]. Based on literature, it is well-known that the increased exposure of conductive Ni sites could enhance the ability of charge transfer in the discharge gap [52]. Additionally, the specific nanosheet structure might be beneficial to generate more surface discharge and charge deposition arising from the two-dimensional structure of Ni/NS- Al_2O_3 catalyst [53]. As expected, the highest time-averaged filamentary current, average number of discharges, average current of the discharge and average lifetime of each discharge were obtained over the Ni/NS- Al_2O_3 sample shown in Fig. S9.

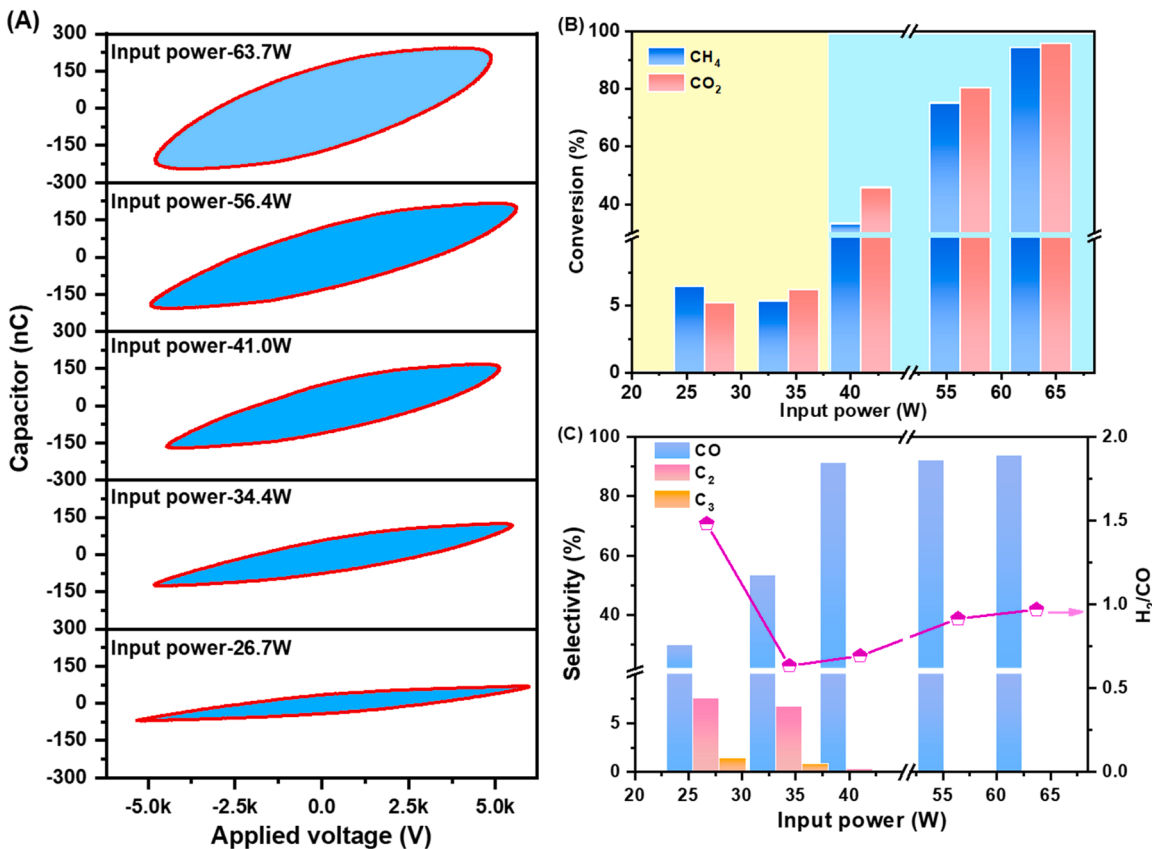


Fig. 5. (A) Q-U Lissajous figures, (B) catalytic activity and (C) carbon products distribution and H₂/CO ratio with different input powers over the Ni/NS-Al₂O₃ catalyst under plasma-catalysis condition. Reaction conditions: WHSV = 600,000 mL/g/h, tube inner diameter 8 mm, m = 0.010 g cat + 0.44 g quartz sand, discharge length 10 mm, CH₄/CO₂/Ar = 3/3/2, the temperature of catalytic bed was ca.113–766 °C with no additional thermal input.

The plasma-catalytic activity for the three Ni/Al₂O₃ catalysts was compared at an input power of ca. 0.55 W under a high WHSV of 600,000 mL/g/h. As shown in Fig. 7(A), the Ni/NR-Al₂O₃ catalyst showed the conversions of CH₄ (20 %) and CO₂ (30 %). And the highest conversions of CH₄ and CO₂ (89 % and 92 %, respectively) were obtained for the Ni/NS-Al₂O₃ catalyst. We could see that the activity differences in trends were similar to the order in catalysis-only condition. The smaller Ni particle size is, the higher activity would be obtained. In contrast, packing quartz sands under plasma-only condition showed very low CH₄ and CO₂ conversions (2.3 % and 1.4 %, respectively), which further suggested that packing catalysts could efficiently promote the improvement of catalytic activity for plasma-assisted DRM reaction. To better understand the synergistic effect between plasma and catalyst, a thermal-catalytic reaction was performed at 760 °C which was chosen based on the temperature measured in the center of the catalyst bed under the plasma-catalytic conditions. While, the Ni/NS-Al₂O₃ catalyst exhibited a much lower conversion of CH₄ and CO₂ (47 % and 60 %, respectively) (Fig. S10). The designed experiments have proved the significantly synergistic effect for plasma coupled with the catalyst in the adiabatic reactor.

C₂ or C₃ hydrocarbons were not detected, and H₂ and CO were dominant products under the evaluated condition. Ni/NS-Al₂O₃ catalyst exhibited the H₂/CO value closed to unity (1.02), while the lowest H₂/CO ratio (0.86) was observed over Ni/NR-Al₂O₃ catalyst due to the contribution from RWGS reaction (Fig. 7(B)), which may result from the formation of larger Ni particle size and further facilitate the RWGS reaction [54]. The energy efficiency (EE) and fuel production efficiency (FPE) as critical parameters were evaluated under plasma-catalytic DRM reaction as shown in Fig. 7(C). Especially, FPE is defined as the energy-to-fuel conversion efficiency in plasma-catalysis system, which is the ratio

of the total energy in produced fuels (H₂ and CO) to the input energy both in plasma and methane feedstock. The highest energy efficiency and fuel production efficiency were obtained with a value of 1.13 mmol/kJ and 36.4 % over Ni/NS-Al₂O₃ catalyst, respectively, which were among the best result to date among the literature (Table S1). It suggests that the high portion of input energy was utilized to produce syngas efficiently over Ni/NS-Al₂O₃ catalyst.

Due to the relatively lower dissociation rate of CO₂ than that of CH₄ in DBD plasma-only reaction, packing catalyst showed a crucial role in CO₂ activation for the plasma-catalytic DRM reaction [55–57]. Therefore, in order to improve stability performance of catalyst, it is vital to enhance the CO₂ dissociation rate to match the fast CH₄ dissociation rate in plasma-catalysis. So, the CO₂ apparent activation energy (E_{a,CO₂}) over Ni/Al₂O₃ catalysts was measured with a WHSV of 1,000,000 mL/g/h in the kinetic region (Table. S2), as shown in Fig. 7(D). The Ni/NS-Al₂O₃ catalyst showed the lowest E_{a,CO₂} of 81.6 kJ/mol, while the Ni/NR-Al₂O₃ catalyst had the highest E_{a,CO₂} of 155 kJ/mol. This was also in accordance with the activity order of the three samples.

Furthermore, the Ni/NS-Al₂O₃ catalyst with the highest activity was chosen to run a stability test in the plasma-catalytic DRM reaction, as shown in Fig. 7(E). The Ni/NS-Al₂O₃ catalyst displayed the high conversions of CH₄ and CO₂ (>95 %) under a WHSV of 100,000 mL/g/h, and the conversions of CH₄ and CO₂ maintained above 90 % within the 50 h time-on stream operation, showing its superior stability performance in the plasma assisted DRM reaction.

3.6. Characterization of the spent Ni/NS-Al₂O₃ catalyst

The spent Ni/NS-Al₂O₃ catalyst after 50 h stability test was characterized by TEM, XRD, Raman and TG-DTA spectra to analyze the degree

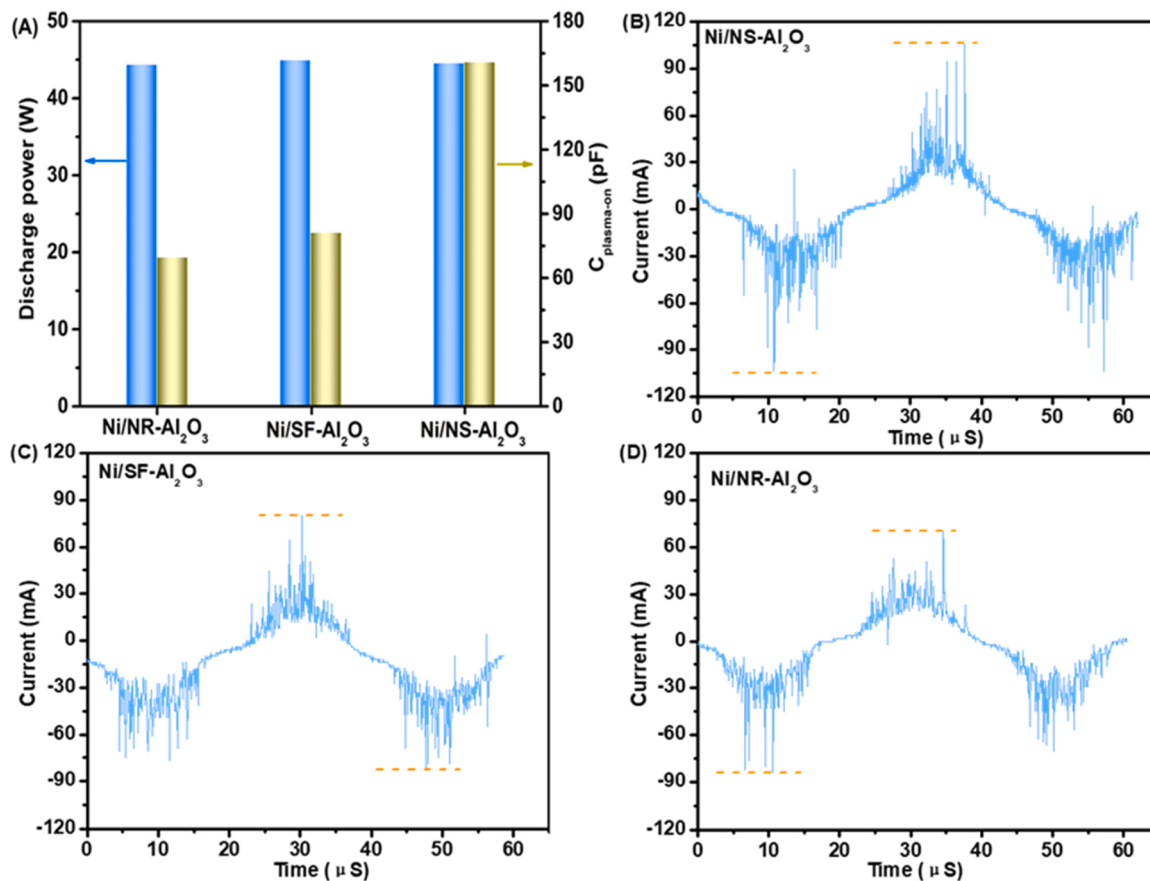


Fig. 6. (A) Discharge power and effective capacitance (Fig. S8); (B-D) Current signals over Ni/Al₂O₃ catalyst with different support morphologies and no external heating in the plasma-catalytic DRM reaction after time-on stream of 200 min. Reaction conditions: WHSV = 600,000 mL/g/h, tube inner diameter 8 mm, m = 0.010 g cat + 0.44 g quartz sand, discharge length 10 mm, input power ca. 55 W, CH₄/CO₂/Ar = 3/3/2, 200 min.

Table 2

The discharge power, effective capacitance and activation energy for CO₂ (E_{a,CO_2}) in plasma-catalytic DRM reaction.

Catalyst	Discharge power (W)	Effective capacitance (pF)	E_{a,CO_2} (kJ/mol)
Ni/NS-Al ₂ O ₃	44.4	161	81.6
Ni/SF-Al ₂ O ₃	44.0	81.0	124
Ni/NR-Al ₂ O ₃	44.6	70.0	155

of metal dispersion and the amount of coke deposition in plasma-assisted DRM reaction (Fig. 8). As shown in Fig. 8(A), the nanosheet structure of the Ni/NS-Al₂O₃ catalyst was preserved under plasma conditions. Also, Ni particles were well dispersed and the average particle size was slightly increased to 7.7 nm (Fig. 8(B)). In addition, there were two types of carbon species observed on the external surface of the spent catalyst, namely amorphous carbon and filamentous carbon. Meanwhile, a stronger diffraction peak of metallic Ni at 44.6° compared that of the reduced Ni/NS-Al₂O₃ (Fig. 8(C)) and a diffraction peak of carbon at 26.6° were also observed in the XRD patterns, suggesting the slight sintering of metallic Ni (JCPDS No. 70-0989) and formation of carbon species (JCPDS No. 26-1080) under long-term stability test. By the Raman spectrum (Fig. 8(D)), a low I_G/I_D ratio of 0.88 was obtained over the spent Ni/NS-Al₂O₃ catalyst, indicating the poor crystallinity of carbon deposited on the spent catalyst. This was consistent with the TGA- DTA result in Fig. 8(E). Moreover, a severe weight loss occurred at ca. 650 °C over the spent catalyst, mainly ascribed to the combustion/oxidation of amorphous and filamentous carbon species [58]. The normalized amounts of carbon deposited on the spent Ni/NA-Al₂O₃

catalyst was 2.21 mmol_{carbon}/mol_{converted CH₄} and CO₂/g_{cat}. The amorphous and filamentous carbon species readily undergo oxidation with CO₂ in the plasma-catalytic process, which may be the reason to explain the good stability performance.

3.7. Discussion

It is generally accepted that the surface defect sites and surface hydroxyl groups on metal oxides (Al₂O₃, SiO₂, TiO₂) played a critical role in tuning metal dispersion by adjusting the strong metal-support interaction [39,44,59]. For example, Kwak et al. revealed that the Pt atom is able to bond to the coordinatively unsaturated Al³⁺ sites on Al₂O₃ support, which acted as metal anchoring sites generated by dehydration and dihydroxylation at 573 K, resulting in the formation of highly dispersed Pt atoms or clusters [35]. Lu et al. also found that the Pt-Sn clusters were highly dispersed and stabilized on a γ-Al₂O₃ nanosheet with 27 % pentacoordinate Al³⁺ sites, and the catalyst exhibited an excellent catalytic activity and high propylene selectivity without metal sintering and coke formation for thermal-catalytic dehydrogenation of propane reaction [21]. On the other hand, Zeng et al. recently revealed that the terminal OH groups on nano-Al₂O₃ surface could act as anchoring sites to obtain Ag-atomic dispersion and enhance the stability of Ag species, therefore a remarkably high catalytic performance was obtained in HC-SCR of NO [39].

In this study, tuning the morphology of Al₂O₃ support from one-dimensional nanorods to two-dimensional nanosheets and three-dimensional spherical-flowers could modify the acidic and basic properties of the catalyst surface, such as Lewis acid sites correspond to pentacoordinate Al³⁺ (Al³⁺_{penta}) and Brønsted acid sites provided by

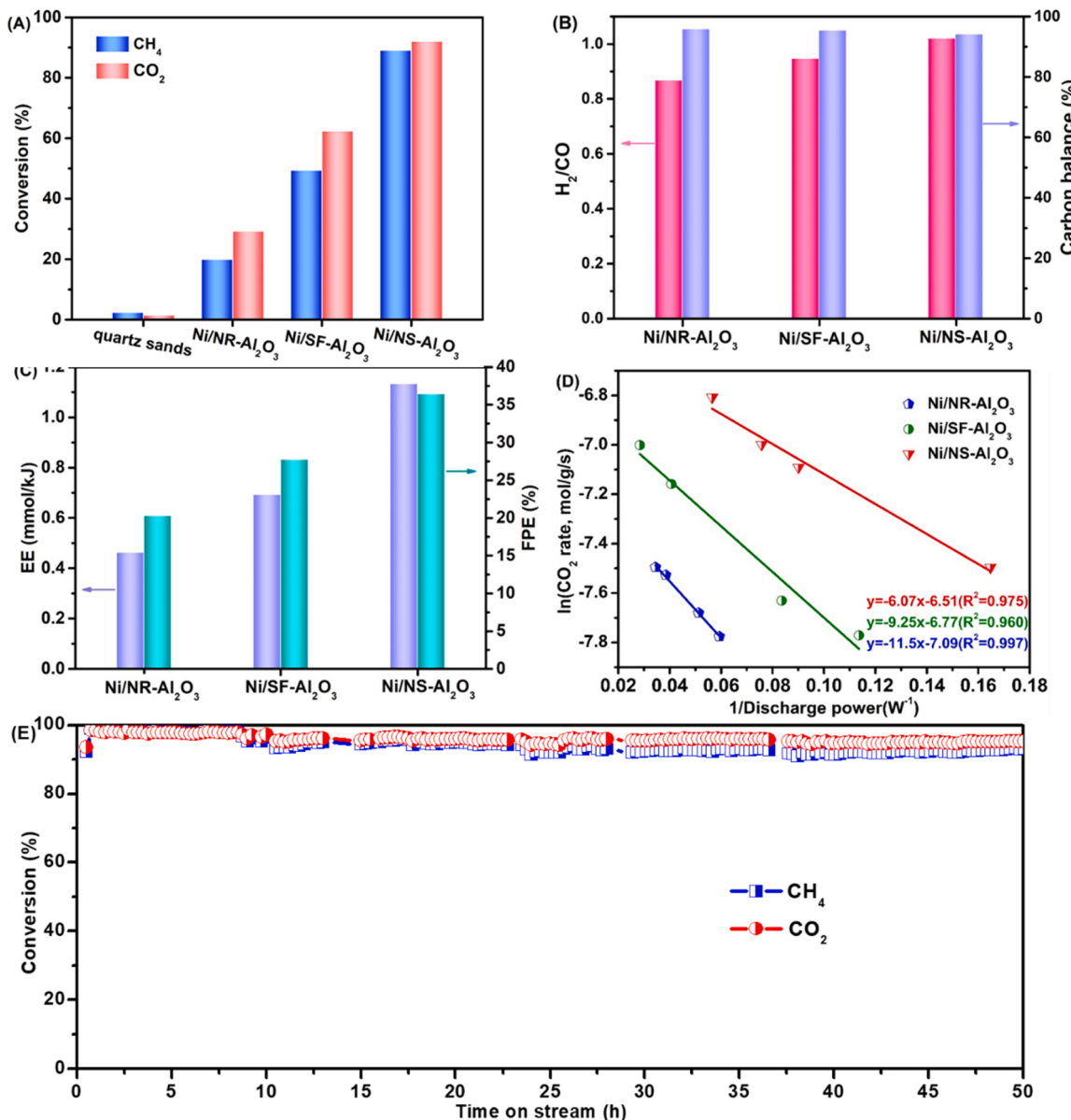


Fig. 7. (A) Conversions of CH₄ and CO₂ over quartz sands and Ni/Al₂O₃ catalysts. (B) H₂/CO ratio and carbon balance; (C) the energy efficiency and the fuel production efficiency over Ni/Al₂O₃ catalyst with different support morphologies and with no external heating in the plasma-catalytic DRM reaction after time-on stream of 200 min. Reaction conditions: WHSV = 600,000 mL/g/h, tube inner diameter 8 mm, m = 0.010 g cat + 0.44 g quartz sand, discharge length 10 mm, input power = ca. 55 W, CH₄/CO₂/Ar = 3/3/2, time-on stream, 200 min (D) Measurements of the apparent activation energy for CO₂ over the Ni/Al₂O₃ catalysts under plasma condition. Reaction conditions: WHSV = 1,000,000 mL/g/h, tube inner diameter 8 mm, m = 0.006 g Cat + 0.444 g quartz sands, discharge length 10 mm, F = 100 mL/min, T = 500 °C, CH₄/CO₂/Ar = 3/3/2. (E) Plasma-catalytic stability performance over Ni/NS-Al₂O₃ catalyst with no external heating in the plasma-catalytic DRM reaction. Reaction conditions: WHSV = 100,000 mL/g/h, tube inner diameter 8 mm, m = 0.060 g Cat + 0.39 g quartz sands, discharge length 10 mm, input power=ca. 55 W, CH₄/CO₂/Ar = 3/3/2.

hydroxyl groups, which could influence the Ni dispersion and the discharge properties of catalysts, and consequently affect the plasma-catalytic performance. For Ni/NS-Al₂O₃ catalyst, the smallest size of metallic Ni (~4.3 nm) was obtained due to a strong interaction between Ni species and sufficient hydroxyl groups on the surface of NS-Al₂O₃ support to anchor Ni species via forming Ni-O-Al bond based on the results of consumption of OH groups after Ni addition [60]. For Ni/SF-Al₂O₃ sample, large amounts of coordinatively unsaturated Al³⁺ acted as anchoring sites for Ni with an average Ni particle size of ca 5.9 nm [35]. In great contrast, the inert surface of NR-Al₂O₃ being lack of bonding sites led to weak metal-support interaction and poor dispersion of Ni particles. Therefore, it could be deduced that the uncoordinated Al³⁺ sites and the hydroxyl groups were of importance to disperse Ni on

Al₂O₃ supports, and the surface properties with different coordination environments of Al³⁺ and surface hydroxyl groups on Al₂O₃ can be precisely turned by different preparation processes.

Ni/Al₂O₃ catalysts with different support morphologies exhibited different discharge behaviors under plasma-assisted DRM reaction. For porous catalysts, many researchers revealed that the generation of plasma was possible in the pore with diameter larger than the Debye length, typically above 3 μm, depending on the electron density and the identity of discharge gas as well as temperature, and limited amount of micro-discharge was formed in pores [61,62]. Nozaki et al. reported that the reactant gas is difficult to breakdown in the discharge region and form excitation states in pores when the pore diameters is below 10 μm, because of the limited collisions between electron and reactant

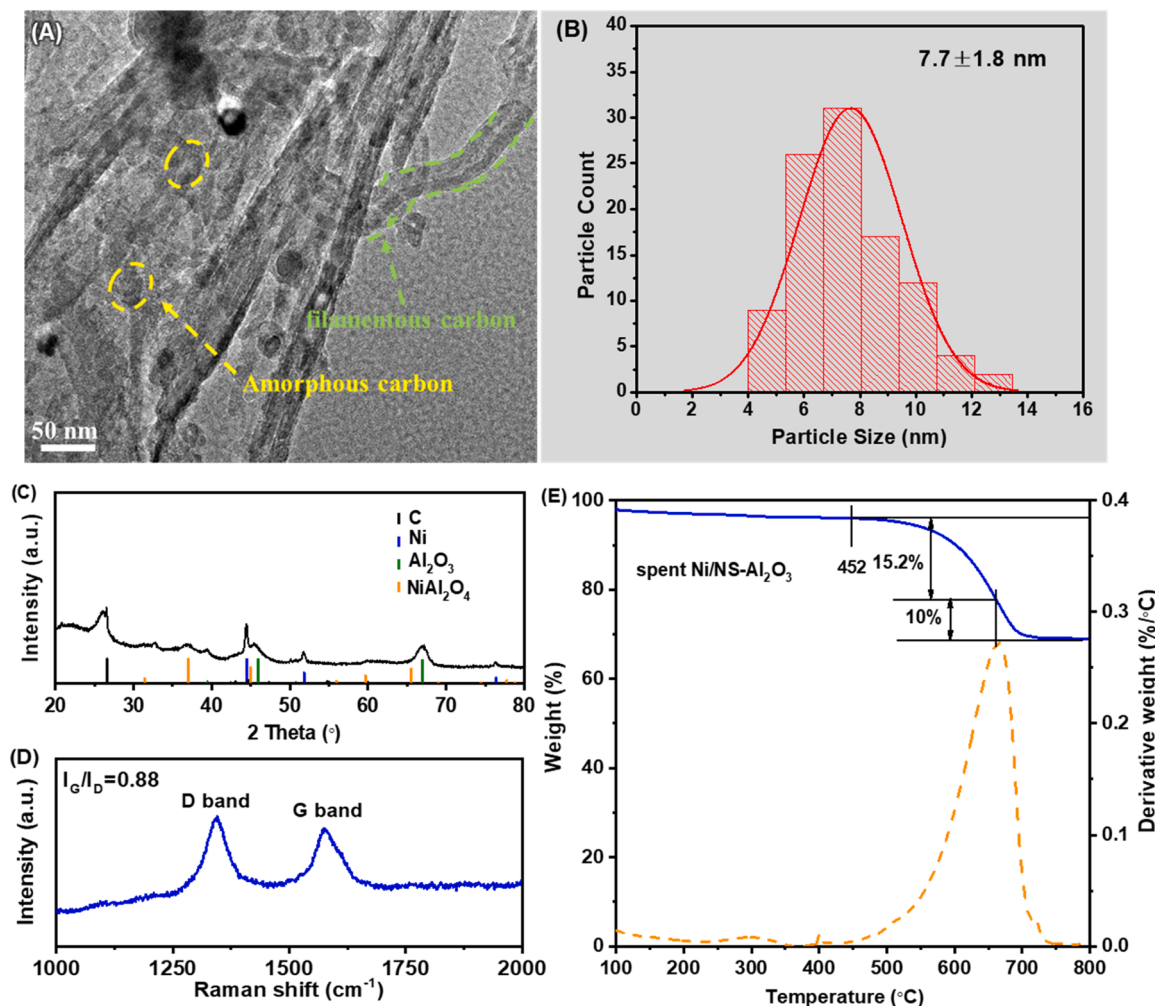


Fig. 8. (A) TEM images and (B) corresponding particle size distribution; (C) XRD pattern, (D) Raman spectrum, (E) TG-DTA plots of the spent Ni/NS-Al₂O₃ catalyst. (Reaction conditions: WHSV = 100,000 mL/g/h, tube inner diameter 8 mm, m = 0.060 g cat + 0.39 g quartz sand, discharge length 10 mm, input power = ca. 55 W, CH₄/CO₂/Ar = 3/3/2, time on stream, 50 h.)

molecules according to the standard Paschen's law [63]. Therefore, the pore size of Al₂O₃ supports with diameter in nanometer scale (<20 nm) has a minor streamer discharge effects. However, the distinct effective capacitance was observed over these three samples. The highest effective capacitance was obtained over Ni/NS-Al₂O₃ catalyst (161 pF), suggesting that more charges were accumulated on the catalyst surface and further formed a stronger local electric field (Table 2).

Furthermore, it is urgent to figure out how the physical properties of applied materials affect the catalytic performances in plasma catalysis? For metal-supported catalyst, it is widely accepted that active metal with good conductivity is beneficial to the expansion of discharge on the catalyst surface under NTP conditions [50,64]. The effective capacitance during the plasma discharge process depends on the spatial discharge distribution of the discharge in the discharge gap [65]. The particle size of metallic Ni showed a direct correlation with effective capacitance. Typically, the smaller Ni size with higher dispersion might enhance the expansion of discharge in the gap, which was considered as "charge bridge" and promoted the charge transfer. This was beneficial to enhance the interaction and synergy between plasma and the catalyst, which further increase the conversions of reactants on surface Ni sites of the catalyst [64]. The stronger local electric field can not only induce the electro-structure changes of the catalysts, but also alter the activation way of reactants. The reactive species such as CH₃^{*}, CH₂^{*}, CH^{*}, CO₂(v) and O^{*} species generated by plasma discharge in the gas phase could get adsorbed on the catalyst surface and incur the chemical reactions.

Moreover, the unique nanosheet morphology with two-dimensional structure of Ni/NS-Al₂O₃ catalyst could facilitate the mass transportation and diffusion both for reactants and products [66,67]. As revealed by Nocaki, the most reactive sites are provided via the interface between plasma and the externally porous Al₂O₃ pellet surface rather than the internal micropores [63]. Therefore, the two-dimensional structure of the Ni/NS-Al₂O₃ catalyst is able to provide more plasma-catalyst interface for plasma-assisted DRM reaction.

Additionally, owing to the balanced rates of CH₄ and CO₂ activation driven by combining plasma and the catalyst, superior stability was obtained at an input power of ca. 50 W under a high WHSV of 100,000 mL/g/h, the conversions can be maintained at above 90 % within 50 h time-on stream operation.

4. Conclusion

Ni/Al₂O₃ catalysts with different support morphologies (nanosheet, spherical flower-like, nanorod) were synthesized and further employed to investigate the effects of support morphology for dry reforming of methane both under thermal- and plasma-catalysis conditions. The surface properties of Al₂O₃ supports were tuned by varying the morphologies. It found that the unsaturated pentacoordinate Al³⁺ and hydroxyl groups sites on Al₂O₃ support are able to stabilize and disperse Ni via binding, resulting in an obviously enhancement on the catalytic performance in DRM reaction. The correlation between Ni particle size

and intrinsic activity (TOF) was established over Ni/Al₂O₃ catalysts under thermal conditions, namely, the TOF value for CH₄ conversion increased with decreasing Ni particle size due to the structure-sensitive nature of the reaction.

For the plasma-catalytic DRM reaction, the effective capacitance and energy efficiency of DBD over different Ni/Al₂O₃ catalysts were affected by Ni particle size and the morphology of the supports. Compared to the Ni/SF-Al₂O₃ and Ni/NR-Al₂O₃ catalysts, the Ni/NS-Al₂O₃ catalyst with the smallest size of Ni and two-dimensional structure showed the lowest activation energy for CO₂. Meanwhile, the Ni/NS-Al₂O₃ catalyst exhibited the highest effective capacitance and energy efficiency during the discharge process, originating from the positive effect of both conductive Ni active sites to promote charge transfer across the discharge gap and enhance the local electron density, and simultaneously the two dimensional structure to facilitate the mass and charge transfer. A superior plasma-catalytic stability was obtained with CH₄ and CO₂ conversions remained above 90 % over Ni/NS-Al₂O₃ catalyst during a 50 h time-on stream operation without external heating. This work provides a promising and practical strategy for developing an efficient Ni-based catalyst with nanosheet-like structure, which can be employed not only for plasma-catalytic DRM reaction but also can be extended to other plasma-catalytic endothermic reactions (such as stream reforming of methane and ammonia decomposition reaction, etc.) at no external heating conditions.

CRediT authorship contribution statement

Yanan Diao: Investigation, Methodology, Data curation, Writing – original draft, Software, Writing – review & editing. **Haiyan Wang:** Data curation, Methodology, Software, Writing – review & editing. **Bingbing Chen:** Data curation, Writing – review & editing. **Xiao Zhang:** Data curation, Formal analysis, Methodology, Software, Writing – review & editing. **Chuan Shi:** Conceptualization, Methodology, Writing – review & editing, Funding acquisition, Supervision, Project administration.

Declaration of Competing Interest

The authors declare that they have no known competing financial interests or personal relationships that could have appeared to influence the work reported in this paper.

Data Availability

Data will be made available on request.

Acknowledgement

The work was supported by the National Key R&D Program of China (No. 2017YFA0700103, 2021YFA1501102), the National Natural Science Foundation of China (No. 21872014, 21932002, 21902018), the Liaoning Revitalization Talent Program (XLYC2008032) and the Fundamental Research Funds for the Central Universities (DUT22ZD212, DUT21RC(3)095, DUT20ZD205, DUT22LAB602). Furthermore, the authors would like to thank the assistance of DUT Instrumental Analysis Center.

Appendix A. Supporting information

Supplementary data associated with this article can be found in the online version at [doi:10.1016/j.apcatb.2023.122573](https://doi.org/10.1016/j.apcatb.2023.122573).

References

- [1] V.V. Thyssen, V.B. Vilela, D.Z. de Florio, A.S. Ferlauto, F.C. Fonseca, Direct conversion of methane to C₂ hydrocarbons in solid-state membrane reactors at high temperatures, *Chem. Rev.* 122 (2022) 3966–3995.
- [2] Y. Tang, Y. Wei, Z. Wang, S. Zhang, Y. Li, L. Nguyen, Y. Li, Y. Zhou, W. Shen, F. F. Tao, P. Hu, Synergy of Single-Atom Ni₁ and Ru₁ Sites on CeO₂ for dry reforming of CH₄, *J. Am. Chem. Soc.* 141 (2019) 7283–7293.
- [3] T. Zhang, Z. Liu, Y.-A. Zhu, Z. Liu, Z. Sui, K. Zhu, X. Zhou, Dry reforming of methane on Ni-Fe-MgO catalysts: influence of Fe on carbon-resistant property and kinetics, *Appl. Catal. B: Environ.* 264 (2020), 118497.
- [4] D. Pakhare, J. Spivey, A review of dry (CO₂) reforming of methane over noble metal catalysts, *Chem. Soc. Rev.* 43 (2014) 7813–7837.
- [5] I.V. Yentekakis, P. Panagiotopoulou, G. Artemakis, A Review of Recent Efforts to Promote Dry Reforming of Methane (DRM) to Syngas Production via Bimetallic Catalyst Formulations, *Appl. Catal. B: Environ.* 296, 2021, p. 120210.
- [6] I.V. Yentekakis, G. Goula, Biogas management: advanced utilization for production of renewable energy and added-value chemicals, *Front. Environ. Sci.* 5 (2017) 7.
- [7] B. AlSabban, L. Falivene, S.M. Kozlov, A. Aguilar-Tapia, S. Ould-Chikh, J.-L. Hazemann, L. Cavallo, J.-M. Basset, K. Takanabe, In-operando elucidation of bimetallic CoNi nanoparticles during high-temperature CH₄/CO₂ reaction, *Appl. Catal. B: Environ.* 213 (2017) 177–189.
- [8] L. Zhou, J.M.P. Martinez, J. Finzel, C. Zhang, D.F. Sweare, S. Tian, H. Robatjazi, M. Lou, L. Dong, L. Henderson, P. Christopher, E.A. Carter, P. Nordlander, N. J. Halas, Light-driven methane dry reforming with single atomic site antenna-reactor plasmonic photocatalyst, *Nat. Energy* (2020) 61–70.
- [9] M. Zhang, J. Zhang, Y. Wu, J. Pan, Q. Zhang, Y. Tan, Y. Han, Insight into the effects of the oxygen species over Ni/ZrO₂ catalyst surface on methane reforming with carbon dioxide, *Appl. Catal. B: Environ.* 244 (2019) 427–437.
- [10] K. Sheng, D. Luan, H. Jiang, F. Zeng, B. Wei, F. Pang, J. Ge, Ni_xCo_y Nanocatalyst Supported by ZrO₂ Hollow Sphere for Dry Reforming of Methane: Synergistic Catalysis by Ni and Co in Alloy, *ACS Appl. Mater. Interfaces* 11 (2019) 24078–24087.
- [11] Y. Gao, J. Jiang, Y. Meng, F. Yan, A. Aihemaiti, A review of recent developments in hydrogen production via biogas dry reforming, *Energ. Convers. Manag.* 171 (2018) 133–155.
- [12] X. Meng, X. Cui, N.P. Rajan, L. Yu, D. Deng, X. Bao, Direct Methane Conversion under Mild Condition by Thermo-, Electro-, or Photocatalysis, *Chem* 5 (2019) 1–30.
- [13] J. Li, L. Dou, Y. Gao, X. Hei, F. Yu, T. Shao, Revealing the active sites of the structured Ni-based catalysts for one-step CO₂/CH₄ conversion into oxygenates by plasma-catalysis, *J. CO₂ Util.* 52 (2021), 101675.
- [14] A.H. Khoja, M. Tahir, N.A.S. Amin, Recent developments in non-thermal catalytic DBD plasma reactor for dry reforming of methane, *Energ. Convers. Manag.* 183 (2019) 529–560.
- [15] X. Wang, J. Wu, J. Wang, H. Xiao, B. Chen, R. Peng, M. Fu, L. Chen, D. Ye, W. Wen, Methanol plasma-catalytic oxidation over CeO₂ catalysts: Effect of ceria morphology and reaction mechanism, *Chem. Eng. J.* 369 (2019) 233–244.
- [16] T. Wang, S. Chen, H. Wang, Z. Liu, Z. Wu, In-plasma catalytic degradation of toluene over different MnO₂ polymorphs and study of reaction mechanism, *Chin. J. Catal.* 38 (2017) 793–803.
- [17] F.F. Holzer, U. Roland, F.D. Kopinke, Combination of non-thermal plasma and heterogeneous catalysis for oxidation of volatile organic compounds Part 1. Accessibility of the intra-particle volume, *Appl. Catal. B: Environ.* 38 (2002) 163–181.
- [18] X. Zhang, Y. Liu, M. Zhang, T. Yu, B. Chen, Y. Xu, M. Crocker, X. Zhu, Y. Zhu, R. Wang, D. Xiao, M. Bi, D. Ma, C. Shi, Synergy between β-Mo₂C Nanorods and Non-thermal Plasma for Selective CO₂ Reduction to CO, *Chem* 6 (2020) 3312–3328.
- [19] H. Chen, F. Goodarzi, Y. Mu, S. Chansai, J.J. Mielby, B. Mao, T. Sooknoi, C. Hardacre, S. Kegnæs, X. Fan, Effect of metal dispersion and support structure of Ni/silicalite-1 catalysts on non-thermal plasma (NTP) activated CO₂ hydrogenation, *Appl. Catal. B: Environ.* 272 (2020), 119013.
- [20] R. Vakili, R. Gholami, C.E. Stere, S. Chansai, H. Chen, S.M. Holmes, Y. Jiao, C. Hardacre, X. Fan, Plasma-assisted catalytic dry reforming of methane (DRM) over metal-organic frameworks (MOFs)-based catalysts, *Appl. Catal. B: Environ.* 260 (2020) 118–195.
- [21] L. Shi, G.M. Deng, W.C. Li, S. Miao, Q.N. Wang, W.P. Zhang, A.H. Lu, Al₂O₃ nanosheets rich in pentacoordinate Al(3+) ions stabilize Pt-Sn clusters for propane dehydrogenation, *Angew. Chem. Int. Ed.* 54 (2015) 13994–13998.
- [22] S. Xu, H. Zhu, W. Cao, Z. Wen, J. Wang, C.P. François-Xavier, T. Wintgens, Cu-Al₂O₃-g-C₃N₄ and Cu-Al₂O₃-C-dots with dual-reaction centres for simultaneous enhancement of Fenton-like catalytic activity and selective H₂O₂ conversion to hydroxyl radicals, *Appl. Catal. B: Environ.* 234 (2018) 223–233.
- [23] F. Wang, J. Zhu, H. Liu, Urea controlled hydrothermal synthesis of ammonium aluminum carbonate hydroxide rods, *AIP Adv.* 8 (2018), 035103.
- [24] Y.X. Zeng, L. Wang, C.F. Wu, J.Q. Wang, B.X. Shen, X. Tu, Low temperature reforming of biogas over K-, Mg- and Ce-promoted Ni/Al₂O₃ catalysts for the production of hydrogen rich syngas: Understanding the plasma-catalytic synergy, *Appl. Catal. B: Environ.* 224 (2018) 469–478.
- [25] J. Kim, D.B. Go, J.C. Hicks, Synergistic effects of plasma-catalyst interactions for CH₄ activation, *Phys. Chem. Chem. Phys.* 19 (2017) 13010–13021.
- [26] S. Xu, S. Chansai, Y. Shao, S. Xu, Y.-C. Wang, S. Haigh, Y. Mu, Y. Jiao, C.E. Stere, H. Chen, X. Fan, C. Hardacre, Mechanistic study of non-thermal plasma assisted CO₂ hydrogenation over Ru supported on MgAl layered double hydroxide, *Appl. Catal. B: Environ.* 268 (2020), 118752.

- [27] F.A. Herrera, G.H. Brown, P. Barboun, N. Turan, P. Mehta, W.F. Schneider, J. C. Hicks, D.B. Go, The impact of transition metal catalysts on macroscopic dielectric barrier discharge (DBD) characteristics in an ammonia synthesis plasma catalysis reactor, *J. Phys. D: Appl. Phys.* 52 (2019), 224002.
- [28] A.L.A. Marinho, F.S. Toniolo, F.B. Noronha, F. Epron, D. Duprez, N. Bion, Highly active and stable Ni dispersed on mesoporous $\text{CeO}_2\text{-Al}_2\text{O}_3$ catalysts for production of syngas by dry reforming of methane, *Appl. Catal. B: Environ.* 281 (2021), 119459.
- [29] H. Zhang, J. Dong, X. Qiao, J. Qin, H. Sun, A. Wang, L. Niu, G. Bai, In-situ generated highly dispersed nickel nanoclusters confined in MgAl mixed metal oxide platelets for benzoic acid hydrogenation, *J. Catal.* 372 (2019) 258–265.
- [30] M. Liao, Y. Chen, Z. Cheng, C. Wang, X. Luo, E. Bu, Z. Jiang, B. Liang, R. Shu, Q. Song, Hydrogen production from partial oxidation of propane: Effect of SiC addition on $\text{Ni}/\text{Al}_2\text{O}_3$ catalyst, *Appl. Energ.* 252 (2019), 113435.
- [31] K. Li, C. Pei, X. Li, S. Chen, X. Zhang, R. Liu, J. Gong, Dry reforming of methane over $\text{La}_2\text{O}_2\text{CO}_3$ -modified $\text{Ni}/\text{Al}_2\text{O}_3$ catalysts with moderate metal support interaction, *Appl. Catal. B: Environ.* 264 (2020), 118448.
- [32] S. Zhang, M. Ying, J. Yu, W. Zhan, L. Wang, Y. Guo, Y. Guo, $\text{Ni}_x\text{Al}_1\text{O}_{2-x}$ mesoporous catalysts for dry reforming of methane: the special role of NiAl_2O_4 spinel phase and its reaction mechanism, *Appl. Catal. B: Environ.* (2021), 120074.
- [33] Q. Yu, T. Yu, H. Chen, G. Fang, X. Pan, X. Bao, The effect of Al^{3+} coordination structure on the propane dehydrogenation activity of $\text{Pt}/\text{Ga}/\text{Al}_2\text{O}_3$ catalysts, *J. Energy Chem.* 41 (2020) 93–99.
- [34] H. Duan, R. You, S. Xu, Z. Li, K. Qian, T. Cao, W. Huang, X. Bao, Pentacoordinated Al^{3+} -stabilized active Pd structures on Al_2O_3 -coated palladium catalysts for methane combustion, *Angew. Chem. Int. Ed.* 58 (2019) 12043–12048.
- [35] J.H. Kwak, J. Hu, D. Mei, C.-W. Yi, D.H. Kim, C.H.F. Peden, L.F. Allard, S. Janos, Coordinatively Unsaturated Al^{3+} centers as binding sites for active catalyst phases of platinum on $\text{g-Al}_2\text{O}_3$, *Science* 325 (2009) 1670–1673.
- [36] X.L.a.R.E.Trutt, DRIFT-IR Studies of the Surface of γ -Alumina, *J. Am. Chem. Soc.* 119, 1997, pp. 9856–9860.
- [37] H. Knözinger, P. Ratnasamy, Catalytic aluminas: surface models and characterization of surface sites, *Catal. Rev.* 17 (1978) 31–70.
- [38] T. Onfroy, W.-C. Li, F. Schuth, H. Knözinger, Surface chemistry of carbon-templated mesoporous aluminas, *Phys. Chem. Chem. Phys.* 11 (2009) 3671–3679.
- [39] F. Wang, J. Ma, S. Xin, Q. Wang, J. Xu, C. Zhang, H. He, X. Cheng Zeng, Resolving the puzzle of single-atom silver dispersion on nanosized gamma- Al_2O_3 surface for high catalytic performance, *Nat. Commun.* 11 (2020) 529.
- [40] M. Heemeier, M. Frank, J. Libuda, K. Wolter, H. Kuhlenbeck, M. Baumer, H.-J. Freund, The influence of OH groups on the growth of rhodium on alumina: a model study, *Catal. Lett.* 68 (2000) 19–24.
- [41] Y. Wang, Y. Hou, X. Hao, Z. Wang, W. Zhu, Effect of metal-doped VPO catalysts for the aldol condensation of acetic acid and formaldehyde to acrylic acid, *RSC Adv.* 9 (2019) 5958–5966.
- [42] S. Yao, Y. Zheng, L. Ding, S. Ng, H. Yang, Co-promotion of fluorine and boron on $\text{NiMo}/\text{Al}_2\text{O}_3$ for hydrotreating light cycle oil, *Catal. Sci. Technol.* 2 (2012) 1925.
- [43] X. Li, C. Wang, S. Liu, W. Xin, Y. Wang, S. Xie, L. Xu, Influences of alkaline treatment on the structure and catalytic performances of ZSM-5/ZSM-11 zeolites with alumina as binder, *J. Mol. Catal. A: Chem.* 336 (2011) 34–41.
- [44] W. Han, B. Liu, Y. Chen, Z. Jia, X. Wei, W. Song, Coordinatively unsaturated aluminum anchored Ru cluster for catalytic hydrogenation of benzene, *J. Catal.* 400 (2021) 255–264.
- [45] J. Wang, Y. Fu, W. Kong, F. Jin, J. Bai, J. Zhang, Y. Sun, Design of a carbon-resistant Ni@S-2 reforming catalyst: Controllable Ni nanoparticles sandwiched in a peacock-like structure, *Appl. Catal. B: Environ.* 282 (2021), 119546.
- [46] N. Wang, K. Shen, L. Huang, X. Yu, W. Qian, W. Chu, Facile route for synthesizing ordered mesoporous Ni-Ce-Al oxide materials and their catalytic performance for methane dry reforming to hydrogen and syngas, *ACS Catal.* 3 (2013) 1638–1651.
- [47] J.W. Han, J.S. Park, M.S. Choi, H. Lee, Uncoupling the size and support effects of Ni catalysts for dry reforming of methane, *Appl. Catal. B: Environ.* 203 (2017) 625–632.
- [48] K. Li, J.-L. Liu, X.-S. Li, X. Zhu, A.-M. Zhu, Warm plasma catalytic reforming of biogas in a heat-insulated reactor: Dramatic energy efficiency and catalyst auto-reduction, *Chem. Eng. J.* 288 (2016) 671–679.
- [49] M. Biset-Péiró, R. Mey, J. Guilera, T. Andreu, Adiabatic plasma-catalytic reactor configuration: Energy efficiency enhancement by plasma and thermal synergies on CO_2 methanation, *Chem. Eng. J.* 393 (2020), 124786.
- [50] X. Tu, H.J. Gallon, M.V. Twigg, P.A. Gorry, J.C. Whitehead, Dry reforming of methane over a $\text{Ni}/\text{Al}_2\text{O}_3$ catalyst in a coaxial dielectric barrier discharge reactor, *J. Phys. D: Appl. Phys.* 44 (2011), 274007.
- [51] H.J. Gallon, X. Tu, J.C. Whitehead, Effects of reactor packing materials on H_2 production by CO_2 reforming of CH_4 in a dielectric barrier discharge, *Plasma Process. Polym.* 9 (2012) 90–97.
- [52] M.M. Gomaa, H.M. Gobara, Electrical properties of Ni/silica gel and $\text{Pt}/\gamma\text{-alumina}$ catalysts in relation to metal content in the frequency domain, *Mater. Chem. Phys.* 113 (2009) 790–796.
- [53] G. Wei, Y. Shen, X. Zhao, Y. Wang, W. Zhang, C. An, Hexagonal phase Ni_3Fe nanosheets toward high-performance water splitting by a room-temperature methane plasma method, *Adv. Funct. Mater.* 32 (2021) 2109709.
- [54] F. Wang, B. Han, L. Zhang, L. Xu, H. Yu, W. Shi, CO_2 reforming with methane over small-sized Ni/SiO_2 catalysts with unique features of sintering-free and low carbon, *Appl. Catal. B: Environ.* 235 (2018) 26–35.
- [55] D. Ray, P.M.K. Reddy, C. Subrahmanyam, $\text{Ni-Mn}/\gamma\text{-Al}_2\text{O}_3$ assisted plasma dry reforming of methane, *Catal. Today* 309 (2018) 212–218.
- [56] A.H. Khoja, M. Tahir, N.A.S. Amin, Cold plasma dielectric barrier discharge reactor for dry reforming of methane over $\text{Ni}/\gamma\text{-Al}_2\text{O}_3\text{-MgO}$ nanocomposite, *Fuel Process. Technol.* 178 (2018) 166–179.
- [57] D. Li, V. Rohani, F. Fabry, A. Parakkulam Ramaswamy, M. Sennour, L. Fulcheri, Direct conversion of CO_2 and CH_4 into liquid chemicals by plasma-catalysis, *Appl. Catal. B: Environ.* 261 (2020) 118–228.
- [58] Y. Diao, X. Zhang, Y. Liu, B. Chen, G. Wu, C. Shi, Plasma-assisted dry reforming of methane over $\text{Mo}_2\text{C-Ni}/\text{Al}_2\text{O}_3$ catalysts: effects of $\beta\text{-Mo}_2\text{C}$ promoter, *Appl. Catal. B: Environ.* 301 (2022), 120779.
- [59] N. Tang, Y. Cong, Q. Shang, C. Wu, G. Xu, X. Wang, Coordinatively unsaturated Al^{3+} sites anchored subnanometric ruthenium catalyst for hydrogenation of aromatics, *ACS Catal.* 7 (2017) 5987–5991.
- [60] Y. Chen, Y. Feng, L. Li, J. Liu, X. Pan, W. Liu, F. Wei, Y. Cui, B. Qiao, X. Sun, X. Li, J. Lin, S. Lin, X. Wang, T. Zhang, Identification of active sites on high-performance $\text{Pt}/\text{Al}_2\text{O}_3$ catalyst for cryogenic CO oxidation, *ACS Catal.* 10 (2020) 8815–8824.
- [61] A. Fridman, *Plasma Chemistry*, Cambridge University Press, New York, 2008.
- [62] Q.-Z. Zhang, W.-Z. Wang, A. Bogaerts, Importance of surface charging during plasma streamer propagation in catalyst pores, *Plasma Sources Sci. Technol.* 27 (2018), 065009.
- [63] S. Kameshima, R. Mizukami, T. Yamazaki, L.A. Prananto, T. Nozaki, Interfacial reactions between DBD and porous catalyst in dry methane reforming, *J. Phys. D: Appl. Phys.* 51 (2018), 114006.
- [64] H.-H. Kim, J.-H. Kim, A. Ogata, Microscopic observation of discharge plasma on the surface of zeolites supported metal nanoparticles, *J. Phys. D: Appl. Phys.* 42 (2009), 135210.
- [65] N. Bouchoul, H. Touati, E. Fourré, J.-M. Clacens, I. Batonneau-Gener, C. Batiot-Dupeyrat, Plasma-catalysis coupling for CH_4 and CO_2 conversion over mesoporous macroporous Al_2O_3 : influence of the physico-chemical properties, *Appl. Catal. B: Environ.* (2021), 120262.
- [66] M. Choi, K. Na, J. Kim, Y. Sakamoto, O. Terasaki, R. Ryoo, Stable single-unit-cell nanosheets of zeolite MFI as active and long-lived catalysts, *Nature* 461 (2009) 246–249.
- [67] Y. Liu, N. Zhao, H. Xian, Q. Cheng, Y. Tan, N. Tsubaki, X. Li, Facilely synthesized H-mordenite nanosheet assembly for carbonylation of dimethyl ether, *ACS Appl. Mater. Interfaces* 7 (2015) 8398–8403.